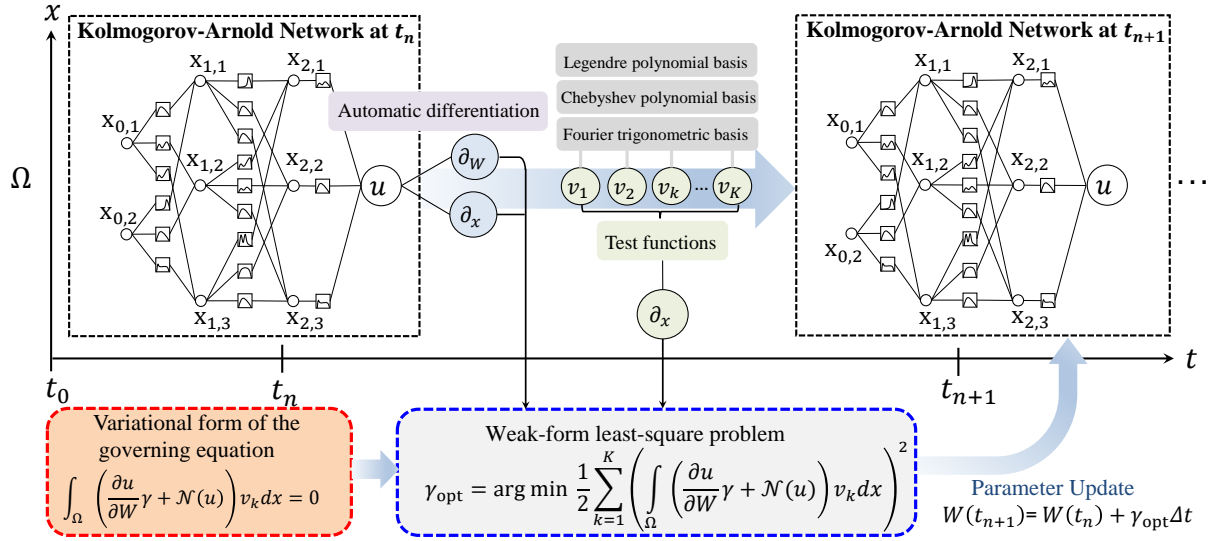


Graphical Abstract

Weak-Form Evolutionary Kolmogorov–Arnold Networks for Solving Partial Differential Equations

Bongseok Kim, Jiahao Zhang, Guang Lin



Highlights

Weak-Form Evolutionary Kolmogorov–Arnold Networks for Solving Partial Differential Equations

Bongseok Kim, Jiahao Zhang, Guang Lin

- A weak-form evolutionary PDE framework improving stability and scalability.
- Fixed-size, well-conditioned parameter updates independent of collocation resolution.
- Dirichlet, periodic, and Neumann boundary conditions consistently incorporated.
- Improved computational efficiency over strong-form approaches.

Weak-Form Evolutionary Kolmogorov–Arnold Networks for Solving Partial Differential Equations

Bongseok Kim^a, Jiahao Zhang^b, Guang Lin^{a,b,*}

^a*Purdue University, School of Mechanical Engineering, West Lafayette, 47906, IN, United States*

^b*Purdue University, Department of Mathematics, West Lafayette, 47906, IN, United States*

Abstract

Partial differential equations (PDEs) form a central component of scientific computing. Among recent advances in deep learning, evolutionary neural networks have been developed to successively capture the temporal dynamics of time-dependent PDEs via parameter evolution. The parameter updates are obtained by solving a linear system derived from the governing equation residuals at each time step. However, strong-form evolutionary approaches can yield ill-conditioned linear systems due to pointwise residual discretization, and their computational cost scales unfavorably with the number of training samples. To address these limitations, we propose a weak-form evolutionary Kolmogorov–Arnold Network (KAN) for the scalable and accurate prediction of PDE solutions. We decouple the linear system size from the number of training samples through the weak formulation, leading to improved scalability compared to strong-form approaches. We also rigorously enforce boundary conditions by constructing the trial space with boundary-constrained KANs to satisfy Dirichlet and periodic conditions, and by incorporating derivative boundary conditions directly into the weak formulation for Neumann conditions. In conclusion, the proposed weak-form evolutionary KAN framework provides a stable and scalable approach for PDEs and contributes to scientific machine learning with potential relevance to future engineering applications.

Keywords: Scientific machine learning, Deep learning, Partial differential equations, Weak formulation, Kolmogorov-Arnold networks, Evolutionary networks

1. Introduction

Deep learning has been explored for approximating solution operators of partial differential equations (PDEs) as well as for representing nonlinear mappings and complex solution manifolds [1, 2, 3], forming an important line of work within scientific machine learning (SciML). Approaches such as the deep Galerkin method (DGM) [4] and physics-informed neural networks (PINNs) [5, 6, 7] formulate PDE learning as a strong-form residual minimization problem and predict the solution of the underlying PDEs. As an extension of PINNs, subsequent extensions have aimed to improve stability, convergence, and the ability to resolve multi-scale features. For instance, adaptive sampling and curriculum strategies [8, 9] redistribute collocation points toward regions with large residuals or sharp gradients, which mitigates training failures on stiff or high-frequency solutions. Domain-decomposition approaches [10, 11], including conservative PINNs and extended PINNs, partition the space–time domain into subdomains that can be trained in parallel and better handle complex geometries and discontinuities. Multi-scale architectures that incorporate Fourier features [12] or multiple frequency components [13] help reduce the spectral bias of standard PINNs and improve accuracy for highly oscillatory solutions. Other extensions address nonlocal operators and fractional dynamics, such as the fractional PINN [14] for space–time fractional advection–diffusion equations.

The deep learning approach has also progressed toward learning solution operators directly, leading to frameworks such as DeepONet [15], the Fourier neural operator (FNO) [16, 17], and the Laplace neural operator (LNO) [18]. Further studies have introduced neural-operator surrogates for PDEs, including methods based on wavelet representations [19] and continuous space–time operator learning [20]. These approaches demonstrate that neural networks can provide mesh-free and generalizable approximations for forward, inverse, and parametric PDE problems.

*Corresponding author

Email addresses: kim4853@purdue.edu (Bongseok Kim), zhan2296@purdue.edu (Jiahao Zhang), guanglin@purdue.edu (Guang Lin)

Along with advances in neural network approaches for solving PDEs, Kolmogorov–Arnold networks (KANs) [21, 22], inspired by the classical representation theorem of Kolmogorov and Arnold [23, 24, 25], have been examined as an alternative to standard multilayer perceptrons (MLPs) in scientific machine learning. While recent works have clarified strengths of MLP-based models, these networks still depend on preset activation functions combined with trainable linear parameters [26, 27]. KANs depart from this structure by replacing fixed activations with trainable spline functions, allowing the network to adjust its nonlinearities locally and to represent features at multiple resolutions [21, 22]. This construction offers advantages in interpretability and provides additional flexibility in representing multivariate mappings. Several studies have explored KAN-based formulations in the context of partial differential equations. Liu et al. [21] embedded KANs within the PINN framework [7] for a two-dimensional Poisson equation, while Abueida et al. [28] introduced DeepOKAN, an operator-learning formulation based on radial-basis representations and evaluated it on two-dimensional orthotropic elasticity and transient diffusion problems. Wang et al. [29] examined KANs across strong-, energy-, and inverse-form PDE formulations within the PIKAN/KINN framework. In addition, Thakolkaran et al. [30] proposed input-convex KAN architectures for hyperelastic constitutive modeling.

Beyond architectural design, another perspective considers how network parameters change when the dynamics vary in time. Models with fixed parameters typically approximate the space–time solution map in one training stage by adding time as an input variable. An alternative perspective is to update the network in a time-marching manner so that the parameters evolve with the temporal dynamics. For instance, Du et al. [31] introduced this idea through the evolutionary deep neural network (EDNN), where the trainable parameters advance according to a time-discretized form of the governing PDE. Their method first trains a baseline network and then propagates its parameters forward in time without repeated optimization. Zhang et al. [32] extended this paradigm to operator learning by applying similar time-marching updates to neural operators for parameterized PDEs. More recent efforts incorporated KAN-based representations into evolutionary schemes. Lin et al. [33] introduced energy-dissipative KANs for solving complex PDE problems, and Kim et al. [34] used Gaussian radial basis functions within the KAN ansatz to enforce boundary constraints during evolution. Despite these developments, existing evolutionary approaches predominantly rely on the strong form of the governing equations, leaving weak-form evolutionary formulations underexplored.

Unlike strong form approaches that enforce PDEs through pointwise residual minimization, weak formulations offer three main advantages: (i) integration by parts reduces the differential order and weakens the regularity requirements, enabling more accurate approximation of discontinuous or steep gradient solutions [35, 36]; (ii) the formulation avoids reliance on high order automatic differentiation, improving numerical stability [37]; and (iii) replacing pointwise collocation constraints with quadrature based integral constraints allows the PDE to be enforced globally with far fewer evaluation points [37]. Within this line of work, Kharazmi et al. [38] introduced the variational physics informed neural network (VPINN) based on a Petrov Galerkin formulation, where the trial space is a neural network and the test space is constructed from classical basis functions. Related extensions, including variational formulations incorporated into operator learning frameworks [39, 40], have reported improved robustness for multi-scale or highly irregular PDE solutions. However, despite these developments, no existing study has applied a variational formulation to evolutionary neural networks.

Inspired by variational approaches for solving PDEs, we propose a weak-form evolutionary framework that incorporates a weak residual formulation into an evolutionary network. We represent the solution on a nonlinear manifold parameterized by boundary-constrained KANs and select polynomial or trigonometric functions as test functions. Specifically, we employ a KAN architecture with Gaussian radial basis functions and impose hard constraints to satisfy the Dirichlet or periodic boundary conditions. To solve the PDE problems, we update the network parameters by solving a weak-form least-squares problem derived from the weak residual of the governing equation, where trigonometric or polynomial test functions define the test space. In contrast to least-squares formulations based on strong forms, the resulting linear system consists of integral terms evaluated over the computational domain, which mitigates pointwise sensitivity, improves numerical stability, and yields more reliable solutions for PDEs with steep or discontinuous features. At each time step, we solve this integral system and advance the network parameters using a forward Euler update. Compared with prior evolutionary network approaches utilizing the strong form, the proposed method provides several advantages:

1. **Scalable computational efficiency** — The proposed weak-form framework decouples the parameter update system size from the number of training samples and fixes it with respect to the number of test functions, resulting in improved scalability compared to strong-form approaches.
2. **Improved conditioning and accuracy** — By reducing the order of differentiation and replacing pointwise residual evaluation with weak residual projections, the proposed method yields well-conditioned linear systems and maintains accuracy for solutions approaching discontinuities.
3. **Rigorous enforcement of boundary conditions** — The proposed method rigorously enforces all types

of boundary conditions: Dirichlet and periodic conditions are imposed through boundary-constrained trial spaces, while Neumann conditions are incorporated directly into the weak formulation via integration by parts.

This paper is organized as follows. Sections 2.1 and 2.2 introduce the network architectures employed in this work. Section 2.3 presents the formulation of the evolutionary Kolmogorov–Arnold network. Section 2.4 describes the proposed weak-form evolutionary approach. Section 3 reports numerical results for representative PDE problems to assess the performance of the method. Finally, Section 4 concludes the study and outlines potential future research directions.

2. Methodology

In this section, we introduce the Kolmogorov–Arnold network (KAN), the KAN enhanced with radial basis functions (RBFs), and the evolutionary KAN formulated in the strong form. We then present the proposed weak-form evolutionary KAN, which reformulates the evolutionary approach in the weak form.

2.1. Kolmogorov–Arnold networks

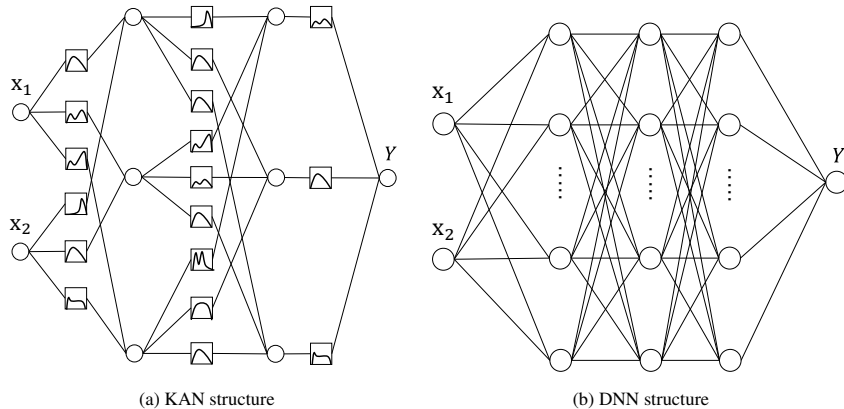


Figure 1: Comparison between the Kolmogorov–Arnold Network (KAN) and a conventional fully connected DNN. (a) The KAN architecture employs functional mappings on each edge, enabling richer nonlinear representations and adaptive feature extraction. (b) The DNN architecture is composed of fully connected layers with activation functions.

Kolmogorov–Arnold networks (KANs) illustrated in Fig. 1(a) place a trainable univariate function on every edge linking two neurons and force each neuron to actively combine transformed edge inputs to produce an output [21, 22]. In comparison, the multilayer perceptrons in a deep neural network (DNN) in Fig. 1(b) impose a single activation function on each layer [41], whereas KANs distribute nonlinear transformations across all connections and thereby yield enhanced expressiveness and interpretability [42]. The Kolmogorov–Arnold theorem establishes a foundation for this architecture by proving that continuous multivariate mappings on bounded domains can be represented through finite sums and compositions of continuous one-dimensional functions [43, 44, 45, 46, 47]. Based on the Kolmogorov–Arnold theorem, a smooth mapping $f : [0, 1]^n \rightarrow \mathbb{R}$ admits the representation

$$f(\mathbf{x}) = \sum_{q=1}^{2n+1} \Phi_q \left(\sum_{p=1}^n \phi_{q,p}(x_p) \right), \quad (1)$$

where each inner mapping $\phi_{q,p} : [0, 1] \rightarrow \mathbb{R}$ modifies a single coordinate and each outer mapping $\Phi_q : \mathbb{R} \rightarrow \mathbb{R}$ merges all contributions. All mappings satisfy continuity conditions imposed by the theorem.

Univariate components in Eq. (1) use third-order B-spline basis functions [21]. The inner stage organizes all one-dimensional mappings into the collection $\Phi = \{\phi_{i,j}\}$ and each element acts on a single coordinate while producing one intermediate channel. The Kolmogorov–Arnold representation fixes the dimensional structure because the first functional stage receives an input of size n and generates $2n + 1$ channels and this requirement yields $n_{\text{in}} = n$ and $n_{\text{out}} = 2n + 1$. A final reduction stage compresses the $2n + 1$ intermediary channels into one scalar through an additional univariate mapping and this step imposes $n_{\text{out}} = 1$ at the terminal stage.

To generalize beyond the canonical n -input and $2n + 1$ -channel structure, this mechanism constructs a hierarchical system of scalar compositions that mirrors the functional representation introduced in Eq. (1). A sequence

of layers is specified by the list $[n_0, n_1, \dots, n_L]$, where n_ℓ denotes the number of neurons in layer ℓ . Each pair of adjacent layers admits one univariate mapping for every directed connection, and the notation

$$\phi_{\ell,j,i}, \quad \ell = 0, \dots, L-1, \quad i = 1, \dots, n_\ell, \quad j = 1, \dots, n_{\ell+1}, \quad (2)$$

indexes all such transformations. Let $x_{\ell,i}$ denote the value produced by the i th neuron in layer ℓ . Then every map consumes $x_{\ell,i}$ and outputs the quantity

$$\tilde{x}_{\ell,j,i} = \phi_{\ell,j,i}(x_{\ell,i}), \quad (3)$$

and neuron j in layer $\ell + 1$ receives the aggregated input

$$x_{\ell+1,j} = \sum_{i=1}^{n_\ell} \tilde{x}_{\ell,j,i} = \sum_{i=1}^{n_\ell} \phi_{\ell,j,i}(x_{\ell,i}), \quad j = 1, \dots, n_{\ell+1}. \quad (4)$$

The transformations in one layer can be collected into a matrix-valued operator

$$\mathbf{\Phi}_\ell = \begin{pmatrix} \phi_{\ell,1,1}(\cdot) & \phi_{\ell,1,2}(\cdot) & \cdots & \phi_{\ell,1,n_\ell}(\cdot) \\ \phi_{\ell,2,1}(\cdot) & \phi_{\ell,2,2}(\cdot) & \cdots & \phi_{\ell,2,n_\ell}(\cdot) \\ \vdots & \vdots & \ddots & \vdots \\ \phi_{\ell,n_{\ell+1},1}(\cdot) & \phi_{\ell,n_{\ell+1},2}(\cdot) & \cdots & \phi_{\ell,n_{\ell+1},n_\ell}(\cdot) \end{pmatrix}, \quad (5)$$

which acts on the vector \mathbf{x}_ℓ through composition, yielding

$$\mathbf{x}_{\ell+1} = \mathbf{\Phi}_\ell \mathbf{x}_\ell. \quad (6)$$

A full KAN applies L such operators in succession so the network output becomes

$$\text{KAN}(\mathbf{x}) = (\mathbf{\Phi}_{L-1} \circ \mathbf{\Phi}_{L-2} \circ \cdots \circ \mathbf{\Phi}_1 \circ \mathbf{\Phi}_0) \mathbf{x}. \quad (7)$$

When the final layer contains a single neuron with $n_L = 1$, the network defines a scalar mapping $f(\mathbf{x})$ and the repeated compositions expand into the following expression:

$$f(\mathbf{x}) = \sum_{i_{L-1}=1}^{n_{L-1}} \phi_{L-1,i_L,i_{L-1}} \left(\sum_{i_{L-2}=1}^{n_{L-2}} \phi_{L-2,i_{L-1},i_{L-2}} \left(\cdots \sum_{i_2=1}^{n_2} \phi_{2,i_3,i_2} \left(\sum_{i_1=1}^{n_1} \phi_{1,i_2,i_1} \left(\sum_{i_0=1}^{n_0} \phi_{0,i_1,i_0}(x_{i_0}) \right) \cdots \right) \right) \right). \quad (8)$$

2.2. Kolmogorov-Arnold networks with radial basis functions

A KAN architecture can adopt RBFs to streamline the construction of univariate transformations and to accelerate numerical operations [48]. The RBFs evaluate a scalar input through a function that depends only on the distance from a fixed center [49, 50]. In particular, the RBFs build an approximation of a target mapping by combining multiple radially symmetric components that concentrate their influence near selected points in the input domain. Incorporating this idea into the KAN framework leads to a representation in which every univariate transformation $\phi_{l,j,i}$ in Eq. (3) is replaced by an RBF expansion of the form

$$\hat{\phi}_{l,j,i}(x) = \sum_{k=1}^g w_{l,j,i}^k \psi(\|x - c_k\|), \quad (9)$$

and this approximation satisfies

$$\phi_{l,j,i}(x) \approx \hat{\phi}_{l,j,i}(x). \quad (10)$$

The coefficients $w_{l,j,i}^k$ determine the contribution of each radial component and the points c_k specify the centers that define the radial distances inside ψ . All layers with indices $l = 0, \dots, L-1$ employ this formulation and every connection from neuron i in layer l to neuron j in layer $l + 1$ adopts the same expansion strategy.

In Eq. (9), the formulation employs Gaussian functions as the radial components, which gives the kernel

$$\psi(r) = \exp\left(-\frac{r^2}{2h^2}\right). \quad (11)$$

The argument r measures the distance from an evaluation point to a specified center, and the parameter h regulates the width and influence of the kernel. Gaussian RBFs, after suitable linear transformations, reproduce sequences of cubic B-spline basis functions [48].

Replacing each univariate mapping in the original construction with an RBF expansion produces an alternative sequence of layer operators. Every operator in this modified sequence uses RBFs $\hat{\phi}_{l,j,i}$ in place of $\phi_{l,j,i}$ and the collection of these approximations forms the transformed layer operators Ψ_l . Applying all such operators in succession defines an RBF-based variant of the architecture and the resulting transformation acting on an input vector \mathbf{x} is given by

$$\text{RBF-KAN}(\mathbf{x}) = (\Psi_{L-1} \circ \Psi_{L-2} \circ \dots \circ \Psi_1 \circ \Psi_0) \mathbf{x}. \quad (12)$$

A single-neuron final layer with $n_L = 1$ converts the network into a scalar-valued mapping. In this situation the output becomes $f(\mathbf{x})$ and the nested structure expands into

$$f(\mathbf{x}) = \sum_{i_{L-1}=1}^{n_{L-1}} \hat{\phi}_{L-1,i_{L-1}} \left(\sum_{i_{L-2}=1}^{n_{L-2}} \hat{\phi}_{L-2,i_{L-1},i_{L-2}} \left(\dots \sum_{i_2=1}^{n_2} \hat{\phi}_{2,i_3,i_2} \left(\sum_{i_1=1}^{n_1} \hat{\phi}_{1,i_2,i_1} \left(\sum_{i_0=1}^{n_0} \hat{\phi}_{0,i_1,i_0}(x_{i_0}) \right) \dots \right) \right) \right). \quad (13)$$

2.3. Evolutionary Kolmogorov–Arnold networks: Strong-form

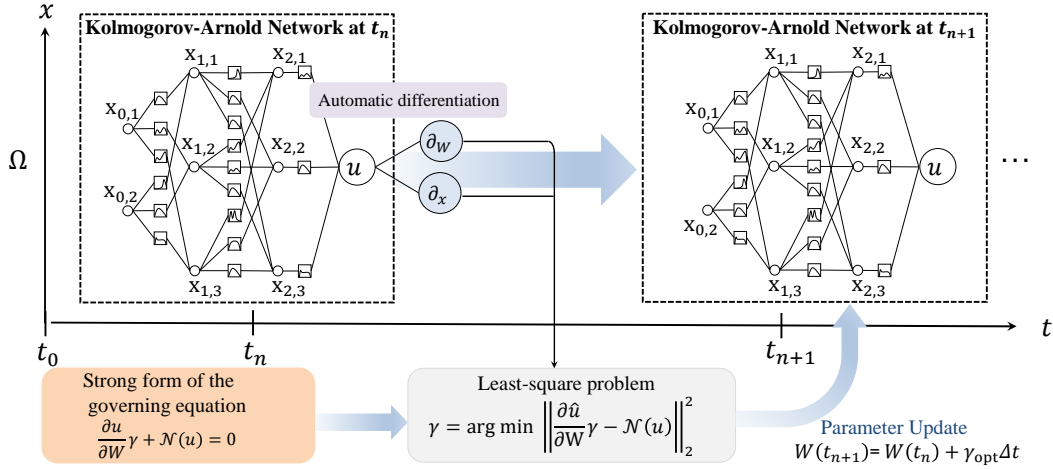


Figure 2: Evolutionary Kolmogorov–Arnold network with Gaussian RBFs: Strong-form formulation. At each time step, the parameters $W(t)$ evolve by minimizing the PDE residual functional $\mathcal{J}(\gamma) = \frac{1}{2} \int_{\Omega} \left\| \frac{\partial \hat{u}}{\partial W} \gamma + \mathcal{N}(\hat{u}) \right\|_2^2 dx$, where the optimal update direction satisfies $\frac{\partial W}{\partial t} = \arg \min_{\gamma} \mathcal{J}(\gamma)$. After obtaining γ_{opt} , the network parameters are explicitly updated in time using the forward Euler scheme $W(t_{n+1}) = W(t_n) + \gamma_{\text{opt}} \Delta t$, yielding a discrete-time parameter evolution associated with the strong-form PDE residual minimization.

This section generalizes the RBF-KAN framework to incorporate an evolutionary learning mechanism [31, 32, 33] to capture the temporal dynamics of PDEs. As a starting point, we consider a general form of a nonlinear PDE accompanied by an initial condition:

$$\begin{aligned} \frac{\partial u}{\partial t} + \mathcal{N}(u) &= 0, \\ u(\mathbf{x}, 0) &= f(\mathbf{x}), \end{aligned} \quad (14)$$

In Eq. (14), the function $u(\mathbf{x}, t) = (u_1, u_2, \dots, u_m)$ represents a multicomponent field, where $\mathbf{x} = (x_1, x_2, \dots, x_d)$ denotes the spatial coordinates, and \mathcal{N} indicates a nonlinear differential operator acting on u .

We now represent the solution u using the RBF-KAN approximation \hat{u} , parameterized by a network with $L + 1$ layers:

$$\hat{u}(\mathbf{x}, W(t)) = (\hat{u}_1, \hat{u}_2, \dots, \hat{u}_m) = \text{RBF-KAN}(\mathbf{x}), \quad (15)$$

where $W(t)$ is a time-dependent vector that collects all trainable parameters of the network. Applying the chain rule yields the following expression for the time derivative of \hat{u} :

$$\frac{\partial \hat{u}}{\partial t} = \frac{\partial \hat{u}}{\partial W} \frac{\partial W}{\partial t}, \quad (16)$$

where the derivative $\frac{\partial W}{\partial t}$ governs the direction of parameter evolution. In the evolutionary network, we require the derivative $\frac{\partial W}{\partial t}$ at each time step. For this purpose, we solve the following optimization problem, where we minimize \mathcal{J} derived from the residual of Eq. (14):

$$\frac{\partial W}{\partial t} = \arg \min_{\gamma} \mathcal{J}(\gamma), \quad \mathcal{J}(\gamma) = \frac{1}{2} \int_{\mathcal{X}} \left\| \frac{\partial \hat{u}}{\partial W} \gamma + \mathcal{N}(\hat{u}) \right\|_2^2 d\mathbf{x}. \quad (17)$$

By the first-order optimality condition, we seek the optimal solution of Eq. (17) by solving the following system:

$$\nabla_{\gamma} \mathcal{J}(\gamma_{\text{opt}}) = \int_{\Omega} \left(\frac{\partial \hat{u}}{\partial W} \right)^T \left(\frac{\partial \hat{u}}{\partial W} \gamma_{\text{opt}} + \mathcal{N}(\hat{u}) \right) d\mathbf{x} = 0. \quad (18)$$

To approximate the solution γ_{opt} to Eq. (18), we recast Eq. (18) into a least-squares formulation as follows:

$$\mathbf{J}^T \mathbf{J} \hat{\gamma}_{\text{opt}} + \mathbf{J}^T \mathbf{N} = 0, \quad (19)$$

Here, \mathbf{J} indicates the sensitivity matrix of the network prediction with respect to trainable parameters, whereas \mathbf{N} denotes the residual values obtained by evaluating the governing equation at selected collocation nodes. The entries of these matrices are defined as follows:

$$(\mathbf{J})_{ij} = \frac{\partial \hat{u}^i}{\partial W_j}, \quad (\mathbf{N})_i = \mathcal{N}(\hat{u}^i), \quad (20)$$

where the index $i = 1, 2, \dots, N_{\hat{u}}$ refers to the evaluation locations and $j = 1, 2, \dots, N_W$ labels the trainable parameters of the network. The entries of both \mathbf{J} and \mathbf{N} are computed using automatic differentiation. After computing γ_{opt} , we update the network parameters using forward Euler method:

$$W(t_{n+1}) = W(t_n) + \gamma_{\text{opt}} \Delta t. \quad (21)$$

We summarize the evolutionary KANs with Gaussian RBFs in Fig. 2 under the strong-form formulation, and delineate the implementation process in Algorithm 1. The network parameters are updated over time in the direction γ derived from the governing PDE, enabling the model to reflect the time-dependent behavior of the solution. Each evolved network state corresponds to a solution snapshot at a given time, and continued updates yield the full solution trajectory.

Algorithm 1 Evolutionary Kolmogorov–Arnold Network: Strong-form

Require: Nonlinear operator \mathcal{N} ; initial condition $f(\mathbf{x})$; collocation points $\{\mathbf{x}^i\}_{i=1}^{N_{\hat{u}}} \subset X$

- 1: **Given:** Time step Δt , number of time steps M , number of collocation points $N_{\hat{u}}$
 - 2: $t_0 \leftarrow 0$
 - 3: Initialize $W(t_0)$ such that $\hat{u}(\mathbf{x}, W(t_0)) \approx f(\mathbf{x})$
 - 4: **for** $n = 0, 1, \dots, M - 1$ **do**
 - 5: Evaluate $\hat{u}^i = \hat{u}(\mathbf{x}^i, W(t_n))$ and store \hat{u}^i together with $W(t_n)$
 - 6: Compute residual entries $N_i^{(n)} = \mathcal{N}(\hat{u}^i)$ and construct the residual vector $N^{(n)}$
 - 7: Compute sensitivity entries $J_{ij}^{(n)} = \frac{\partial \hat{u}^i}{\partial W_j}$ and construct the sensitivity matrix $J^{(n)}$
 - 8: Solve $J^{(n)T} J^{(n)} \gamma_{\text{opt}}^{(n)} = -J^{(n)T} N^{(n)}$ for $\gamma_{\text{opt}}^{(n)}$
 - 9: Update $W(t_{n+1}) \leftarrow W(t_n) + \Delta t \gamma_{\text{opt}}^{(n)}$
 - 10: **end for**
 - 11: **return** $\{W(t_n)\}_{n=0}^M$ and $\{\hat{u}(\mathbf{x}, W(t_n))\}_{n=0}^M$
-

2.4. Evolutionary Kolmogorov–Arnold networks: Weak-form

2.4.1. Trial space: Boundary-constrained KAN

To construct a trial space that satisfies boundary conditions by network design, the boundary constraints are incorporated directly into the basis functions of the evolutionary KAN. With this construction, all admissible functions generated by the trial space inherently satisfy the Dirichlet and periodic boundary conditions, independent of the trainable parameters. Neumann boundary conditions are enforced during the evolutionary stage by incorporating them directly into the weak-form. Further details on boundary-constrained KAN architectures can be found in [34].

For homogeneous Dirichlet boundaries, the KAN architecture employs two types of scaling functions. At the first hidden layer, each basis function constructed from Gaussian RBFs is multiplied by a factor that vanishes on the boundary. A representative choice is

$$h_1(\mathbf{x}) = \prod_{i=1}^d (x_i - k_i)^{p_i}, \quad 0 < p_i \leq 1, \quad (22)$$

and this factor forces every basis response to be zero whenever \mathbf{x} lies on the domain boundary. In the subsequent layers, activations are rescaled by a second map that preserves zero values,

$$h_2(z) = z^q, \quad 0 < q \leq 1. \quad (23)$$

Once a zero value appears at some layer, later layers maintain the zero value under this scaling, and the prediction $\hat{u}(\mathbf{x})$ therefore satisfies the homogeneous Dirichlet condition on the boundary. In the case of non-homogeneous boundary conditions, a lifting function $l(\mathbf{x}, t)$ is introduced, leading to the following trial function:

$$u(\mathbf{x}; W(t)) = \hat{u}(\mathbf{x}; W(t)) + l(\mathbf{x}, t). \quad (24)$$

For periodic boundary conditions, the spatial coordinates are first mapped to a periodic feature representation. For instance, a one-dimensional coordinate x can be embedded using multiple Fourier components,

$$x \mapsto (\sin(\omega x), \cos(\omega x), \sin(2\omega x), \cos(2\omega x), \dots), \quad \omega = \frac{2\pi}{L}, \quad (25)$$

and the number of harmonics is selected according to the spectral content of the target function. The periodic feature representation satisfies the boundary identity, and any function produced by composing these features with the KAN layers preserves finite-order periodicity,

$$u^{(\ell)}(a) = u^{(\ell)}(b), \quad 0 \leq \ell \leq k, \quad (26)$$

where k corresponds to the highest spatial derivative order in the PDE. For multidimensional problems, each coordinate is independently embedded through the same periodic mapping, and the resulting feature vectors are concatenated prior to evaluation by the radial basis layers.

2.4.2. Weak-form evolutionary Kolmogorov–Arnold networks

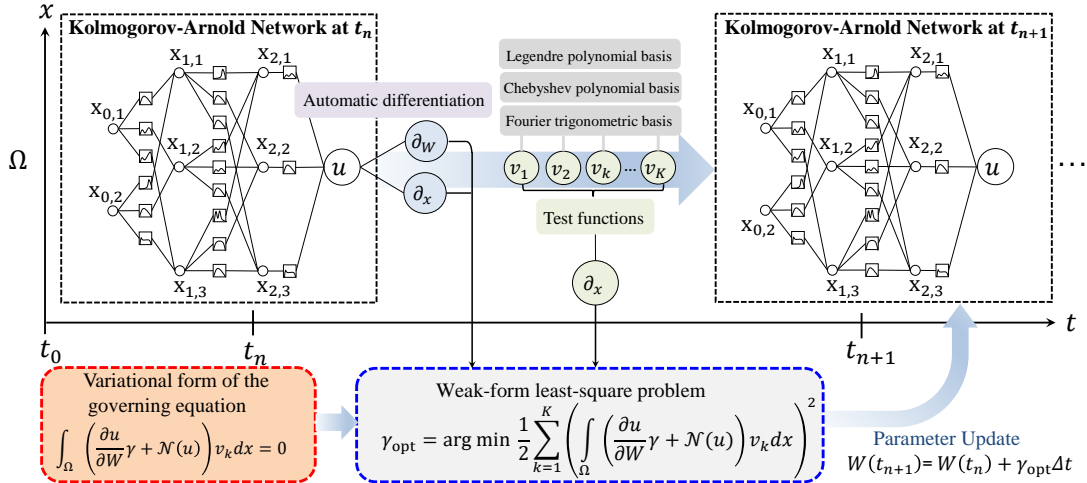


Figure 3: Weak-form evolutionary Kolmogorov–Arnold network. At each time step, the parameters $W(t)$ are updated by minimizing the weak-form residual functional $\mathcal{J}(\gamma) = \frac{1}{2} \sum_{k=1}^K \left(\int_{\Omega} \left(\frac{\partial u}{\partial W} \gamma + \mathcal{N}(u) \right) v_k dx \right)^2$, where $\{v_k\}_{k=1}^K$ denote the test functions. The optimal update direction is given by $\gamma_{\text{opt}} = \arg \min_{\gamma} \mathcal{J}(\gamma)$, and the network parameters are advanced in time via the forward Euler step $W(t_{n+1}) = W(t_n) + \gamma_{\text{opt}} \Delta t$, resulting in a discrete-time parameter evolution associated with the weak-form residual minimization.

A weak-form evolutionary KAN framework approximates the parameter evolution of time-dependent PDEs by enforcing the governing equation in an integral sense. The overall structure of this weak-form update process is summarized schematically in Fig. 3. Consider a nonlinear evolution problem of the form

$$\frac{\partial u}{\partial t}(x, t) + \mathcal{N}(u(x, t)) = 0, \quad u(x, 0) = u_0(x), \quad (27)$$

where $t \in [0, T]$, $x \in \Omega \subset \mathbb{R}^d$, and $u(x, t)$ denotes the unknown state field. The operator \mathcal{N} represents a nonlinear differential operator in space acting on u , and $u_0(x)$ specifies the prescribed initial condition at $t = 0$.

In the evolutionary network setting, the solution u is approximated by a parametric model $\hat{u}(x, W(t))$, where the parameter vector $W(t) \in \mathbb{R}^p$ evolves in time. The temporal evolution of $W(t)$ is described by an auxiliary vector γ through the relation

$$\frac{\partial \hat{u}}{\partial t}(x, t) = \frac{\partial \hat{u}}{\partial W}(x, W(t)) \gamma, \quad (28)$$

Algorithm 2 Evolutionary Kolmogorov-Arnold Network: Weak-form

Require: Nonlinear operator \mathcal{N} ; test functions $\{v_k\}_{k=1}^K$; domain Ω ; quadrature nodes $\{x_i, w_i\}_{i=1}^{N_x}$; initial condition $u_0(x)$

- 1: **Given:** time step Δt , number of time steps M , parameter dimension P
 - 2: Initialize $W(t_0)$ such that $u(x, W(t_0)) \approx u_0(x)$
 - 3: **for** $n = 0, 1, \dots, M - 1$ **do**
 - 4: Evaluate $u^i = \hat{u}(x_i, W(t_n))$ and store \hat{u}^i together with $W(t_n)$
 - 5: Compute weak-form sensitivity entries $J_{kj} = \sum_{i=1}^{N_x} w_i \frac{\partial \hat{u}}{\partial W_j}(x_i) v_k(x_i)$
 - 6: Compute weak-form residual entries $N_k = \sum_{i=1}^{N_x} w_i \mathcal{N}(\hat{u}(x_i)) v_k(x_i)$
 - 7: Assemble $J^{(n)}$ from the rows (J_{k1}, \dots, J_{kP})
 - 8: Assemble $N^{(n)}$ from entries N_k
 - 9: Solve $J^{(n)\top} J^{(n)} \gamma_{\text{opt}}^{(n)} = -J^{(n)\top} N^{(n)}$
 - 10: Update $W(t_{n+1}) \leftarrow W(t_n) + \Delta t \gamma_{\text{opt}}^{(n)}$
 - 11: **end for**
 - 12: **return** $\{W(t_n)\}_{n=0}^M$ and $\{u(\mathbf{x}, W(t_n))\}_{n=0}^M$
-

and substitution into the governing equation defines the residual

$$R(x; W, \gamma) = \frac{\partial \hat{u}}{\partial W}(x, W) \gamma + \mathcal{N}(\hat{u}(x, W)). \quad (29)$$

To construct a weak formulation, a finite collection of test functions $\{v_k\}_{k=1}^K$ on Ω is introduced. In all experiments, we employ low-order polynomial or trigonometric bases whose cardinality is chosen to adequately resolve the dominant spatial modes of the solution. Empirically, we observe that once K exceeds the effective modal complexity of the solution, further increases in K lead to only marginal improvements. For each v_k , the residual is projected in a weak sense by integrating over the spatial domain:

$$\int_{\Omega} R(x; W, \gamma) v_k(x) dx = \int_{\Omega} \left(\frac{\partial u}{\partial W}(x, W) \gamma + \mathcal{N}(u(x, W)) \right) v_k(x) dx \approx 0, \quad k = 1, \dots, K. \quad (30)$$

These conditions enforce the PDE in a weak sense along the directions spanned by the test functions, which can reduce the influence of high-frequency components in the residual.

The direction γ is determined by minimizing a least-squares functional that aggregates the weak residuals over the entire test set. Specifically, the optimal update direction is obtained as

$$\gamma_{\text{opt}} = \arg \min_{\gamma} J(\gamma), \quad J(\gamma) = \frac{1}{2} \sum_{k=1}^K \left(\int_{\Omega} \left(\frac{\partial u}{\partial W}(x, W) \gamma + \mathcal{N}(u(x, W)) \right) v_k(x) dx \right)^2. \quad (31)$$

Each term in the sum represents the squared weak residual associated with a single test function, and the functional $J(\gamma)$ quantifies the overall weak residual. The first-order optimality condition for this minimization problem requires the gradient of J with respect to γ to vanish. The gradient can be written as

$$\nabla_{\gamma} J(\gamma) = \sum_{k=1}^K \left[\int_{\Omega} \left(\frac{\partial u}{\partial W}(x, W) \gamma + \mathcal{N}(u(x, W)) \right) v_k(x) dx \right] \left[\int_{\Omega} \frac{\partial u}{\partial W}(x, W) v_k(x) dx \right] = 0. \quad (32)$$

This expression indicates that the optimal direction γ must balance the weak residuals and their sensitivities with respect to the parameters.

To obtain an explicit algebraic form, introduce for each test function v_k the row vector $J_k \in \mathbb{R}^P$ and scalar N_k defined by

$$J_{kj} = \int_{\Omega} \frac{\partial u}{\partial W_j}(x, W) v_k(x) dx, \quad N_k = \int_{\Omega} \mathcal{N}(u(x, W)) v_k(x) dx, \quad 1 \leq k \leq K, 1 \leq j \leq P. \quad (33)$$

The vector J_k collects the weak sensitivities of the network output with respect to each parameter W_j under the test function v_k , while N_k captures the weak projection of the PDE residual under the test function $v_k(x)$. With these definitions, the optimality condition can be rewritten in compact index notation as

$$\sum_{k=1}^K \left[\underbrace{\left(\int_{\Omega} \frac{\partial u}{\partial W}(x, W) v_k(x) dx \right)^T}_{J_k^T} \left(\underbrace{\int_{\Omega} \frac{\partial u}{\partial W}(x, W) v_k(x) dx}_{J_k \gamma} \gamma + \underbrace{\int_{\Omega} \mathcal{N}(u(x, W)) v_k(x) dx}_{N_k} \right) \right] = 0. \quad (34)$$

The above representation clarifies that the linearization of the objective around γ involves only inner products between the sensitivity vectors and the projected residuals.

In practical computation, the spatial integrals defining J_{kj} and N_k are evaluated numerically. Using Gauss–Legendre quadrature on Ω with nodes $\{x_i\}_{i=1}^{N_x}$ and weights $\{w_i\}_{i=1}^{N_x}$ leads to the approximations

$$J_{kj} = \int_{\Omega} \frac{\partial u}{\partial W_j}(x, W) v_k(x) dx \approx \sum_{i=1}^{N_x} w_i \frac{\partial u}{\partial W_j}(x_i, W) v_k(x_i), \quad (35)$$

$$N_k = \int_{\Omega} \mathcal{N}(u(x, W)) v_k(x) dx \approx \sum_{i=1}^{N_x} w_i \mathcal{N}(u(x_i, W)) v_k(x_i). \quad (36)$$

These formulas express each entry of J_k and N_k as a weighted sum over collocation points and provide a discrete representation compatible with automatic differentiation for $\partial u / \partial W_j$.

Stacking the rows J_k into a matrix

$$J = \begin{pmatrix} J_1^T \\ \vdots \\ J_K^T \end{pmatrix} \in \mathbb{R}^{K \times P}, \quad N = \begin{pmatrix} N_1 \\ \vdots \\ N_K \end{pmatrix} \in \mathbb{R}^K, \quad (37)$$

the optimality condition becomes the normal equation

$$J^T J \gamma_{\text{opt}} = -J^T N. \quad (38)$$

Here, K denotes the number of test functions and P denotes the number of trainable parameters in the network. The matrix $J^T J \in \mathbb{R}^{P \times P}$ and vector $J^T N \in \mathbb{R}^P$ define a linear system for the update direction γ_{opt} . Solving this system yields the parameter evolution direction that minimizes the weak-form residual in the least-squares sense for the chosen set of test functions and quadrature nodes. The number of test functions K is selected to balance expressive power and numerical stability. The equation form $J^T J \gamma = -J^T N$ in Eq. (38) is adopted for consistency with existing evolutionary-network formulations and for notational clarity. Although solving normal equations may amplify conditioning issues in general, our numerical results indicate that the weak-form projection substantially improves conditioning compared to strong-form enforcement. Alternative solvers based on QR or SVD factorizations, as well as Tikhonov regularization, are fully compatible with the proposed framework and can be employed when higher numerical robustness is required.

2.4.3. Computational complexity

Table 1 compares the dominant computational costs of strong-form and weak-form evolutionary approaches over M time steps. The analysis focuses on the per-step evaluation of the residual N and sensitivity matrix J , as well as on the solution of the parameter-update least-squares problem, and reports their leading-order asymptotic scaling.

In the strong-form approach, the least-squares problem is posed over $N_{\hat{u}}$ collocation points, yielding a Jacobian $J \in \mathbb{R}^{N_{\hat{u}} \times P}$. At each time step, the PDE residual is evaluated pointwise, requiring higher-order spatial derivatives and incurring a cost $\mathcal{O}(N_{\hat{u}} C_{\text{PDE}}^{\text{SF}})$. Automatic differentiation is applied at all collocation points to assemble the J , with cost $\mathcal{O}(N_{\hat{u}} P C_{\text{AD}})$. Assuming a dense least-squares solve, the per-step solution cost scales as $\mathcal{O}(N_{\hat{u}} P^2)$. The cumulative cost over M time steps is therefore

$$\mathcal{O}\left(M \left(N_{\hat{u}} P^2 + N_{\hat{u}} P C_{\text{AD}} + N_{\hat{u}} C_{\text{PDE}}^{\text{SF}} \right)\right), \quad (39)$$

indicating that both the system dimension and residual evaluation cost grow with the number of collocation points.

In the weak-form approach, the residual is projected onto a fixed set of K test functions, resulting in a parameter-update system $J \in \mathbb{R}^{K \times P}$ whose size is independent of the data resolution. The PDE residual is evaluated at N_x quadrature points, with reduced differential order due to integration by parts, leading to a cost $\mathcal{O}(N_x C_{\text{PDE}}^{\text{WF}})$. Automatic differentiation at quadrature points yields a Jacobian assembly cost of $\mathcal{O}(N_x P C_{\text{AD}})$. Projection onto the test space introduces additional integration costs: $\mathcal{O}(K N_x)$ for assembling the weak residual and $\mathcal{O}(K N_x P)$ for constructing the projected Jacobian. The per-step least-squares system formation scales as $\mathcal{O}(K P^2)$, and the total cost over M time steps becomes

$$\mathcal{O}\left(M \left(K P^2 + N_x P C_{\text{AD}} + N_x C_{\text{PDE}}^{\text{WF}} + K N_x P + K N_x \right)\right). \quad (40)$$

Typically, the number of strong-form collocation points satisfies $N_{\hat{u}} \gg K$, whereas in the weak formulation the projection is evaluated using a similar number of quadrature points N_x as the collocation points $N_{\hat{u}}$, while the

Table 1: Computational complexity comparison of strong-form and weak-form evolutionary solvers over M time steps. Here $J = \partial\hat{u}/\partial W$ and $N = \mathcal{N}(\hat{u})$ denote the parameter Jacobian and PDE residual. $N_{\hat{u}}$ and N_x are the numbers of collocation and quadrature points, K the number of test functions, and P the number of trainable parameters. C_{AD} denotes parameter automatic differentiation cost, while C_{PDE} denotes spatial differentiation cost for residual evaluation. Due to integration by parts, C_{PDE}^{WF} is lower than C_{PDE}^{SF} .

	Strong form	Weak form
System to solve	$J^T (P \times N_{\hat{u}}) J (N_{\hat{u}} \times P) \gamma_{\text{opt}} = -J^T (P \times N_{\hat{u}}) N (N_{\hat{u}} \times 1)$	$J^T (P \times K) J (K \times P) \gamma_{\text{opt}} = -J^T (P \times K) N (K \times 1)$
Data–system coupling	Coupled: system size scales with $N_{\hat{u}}$	Decoupled: system size fixed by K
J evaluation	$O(N_{\hat{u}} P C_{AD})$	$O(N_x P C_{AD} + KN_x P)$
N evaluation	$O(N_{\hat{u}} C_{PDE}^{SF})$	$O(N_x C_{PDE}^{WF} + KN_x)$
Least-squares system formation	$O(N_{\hat{u}} P^2)$	$O(KP^2)$
Total cumulative cost	$O\left(M\left(N_{\hat{u}} P^2 + N_{\hat{u}} P C_{AD} + N_{\hat{u}} C_{PDE}^{SF}\right)\right)$	$O\left(M\left(KP^2 + N_x P C_{AD} + N_x C_{PDE}^{WF} + KN_x P + KN_x\right)\right)$

dimension of the resulting update system remains governed by the number of test functions K . As a result, the weak-form evolutionary solver exhibits more favorable scaling, with additional data primarily improving projection accuracy rather than increasing the cost of the parameter-update system. We emphasize that the computational advantage of the proposed weak-form evolutionary solver lies in decoupling the parameter-update system size from the number of quadrature points. While increasing N_x improves the accuracy of weak residual evaluation, it does not alter the dimension of the least-squares system, which remains fixed by the number of test functions K .

3. Numerical Experiments

In this section, three approaches are compared: (i) EvoKAN-WF (Evolutionary KAN with weak-form, Sec. 2.4), (ii) EvoKAN-SF (Evolutionary KAN with strong-form, Sec. 2.3), (iii) a standard PINN-SF [51] (PINN with strong-form). EvoKAN-WF adopts a weak formulation in which the residual is projected onto a finite set of test functions, using Gaussian RBFs together with the boundary-constrained KAN described in Sec. 2.4.1. EvoKAN-SF employs the same Gaussian RBFs architecture and boundary construction but enforces the governing equation in the strong form at collocation points. The PINN-SF baseline is trained over the entire spatio-temporal domain and applies boundary conditions through soft penalty terms without an evolutionary update in time. Regarding computational resources, an NVIDIA GeForce RTX 4090 GPU was used for initial condition training, while parameter evolution ran on an AMD Threadripper PRO 5955WX with 31 cores.

3.1. 1D Allen-Cahn equation

The one-dimensional Allen–Cahn equation considered in this numerical experiment is

$$\frac{\partial u}{\partial t} = \frac{\partial^2 u}{\partial x^2} - \frac{1}{\epsilon^2} u(u^2 - 1), \quad x \in [-1, 1], t \geq 0, \quad (41)$$

where the parameter $\epsilon = 0.002$ controls the thickness of the diffuse interface. Smaller values of ϵ produce sharper transition layers, resulting in a stiff nonlinear reaction term and rapid changes in the solution profile.

The initial condition is given by

$$u(x, 0) = 0.08 \sin(\pi x), \quad (42)$$

and homogeneous Dirichlet boundary conditions are imposed:

$$u(-1, t) = 0, \quad u(1, t) = 0. \quad (43)$$

To derive the weak formulation, the PDE is multiplied by a test function v_k and integrated over the spatial domain:

$$\int_{\Omega} \frac{\partial u}{\partial t} v_k dx = \int_{\Omega} \frac{\partial^2 u}{\partial x^2} v_k dx - \int_{\Omega} \frac{1}{\epsilon^2} u(u^2 - 1) v_k dx. \quad (44)$$

The diffusion term is treated by integration by parts:

$$\int_{\Omega} \frac{\partial^2 u}{\partial x^2} v_k dx = - \int_{\Omega} \frac{\partial u}{\partial x} \frac{\partial v_k}{\partial x} dx + \left[\frac{\partial u}{\partial x} v_k \right]_{x=-1}^{x=1}. \quad (45)$$

Because the test functions satisfy $v_k(\pm 1) = 0$, the boundary contribution vanishes, and the weak form of the Allen–Cahn equation becomes

$$\int_{\Omega} \frac{\partial u}{\partial t} v_k dx = - \int_{\Omega} \frac{\partial u}{\partial x} \frac{\partial v_k}{\partial x} dx - \int_{\Omega} \frac{1}{\epsilon^2} u(u^2 - 1) v_k dx, \quad k = 1, \dots, K. \quad (46)$$

In the numerical experiments, the test functions v_k are chosen as sinusoidal functions on $[-1, 1]$ of the form $v_k(x) = \sin(k\pi(x + 1)/2)$, $k = 1, \dots, K$, which satisfy $v_k(-1) = v_k(1) = 0$ by construction and provide increasing spatial frequency as k increases. Unless otherwise specified, all weak-form integrals are evaluated using Gauss–Legendre quadrature with N_x nodes per spatial dimension. We verified that moderate increases in N_x lead to negligible changes in solution accuracy, confirming that the dominant computational cost is governed by K rather than the quadrature resolution.

We summarize the training settings for EvoKAN-WF, EvoKAN-SF, and PINN-SF in Table 2. EvoKAN-WF and EvoKAN-SF employ the same network architecture and are trained for the initial condition using the Adam optimizer, followed by time marching via parameter evolution with a fixed time step. In contrast, PINN-SF uses a deeper MLP with \tanh activations and is trained using Adam/L-BFGS-B without explicit time evolution.

Table 2: Training configuration for the 1D Allen-Cahn equation (Eq. (41)).

	EvoKAN-WF	EvoKAN-SF	PINN-SF
Hidden layers	[3, 3, 3, 3]	[3, 3, 3, 3]	[15, 15, 15]
Activation functions	Gaussian RBFs/SiLU	Gaussian RBFs/SiLU	Tanh
Grid points number of activation functions	4	4	-
Number of trainable parameters	162	195	526
Optimizer	Adam	Adam	Adam/L-BFGS-B
Timestep	1e-07	1e-07	-

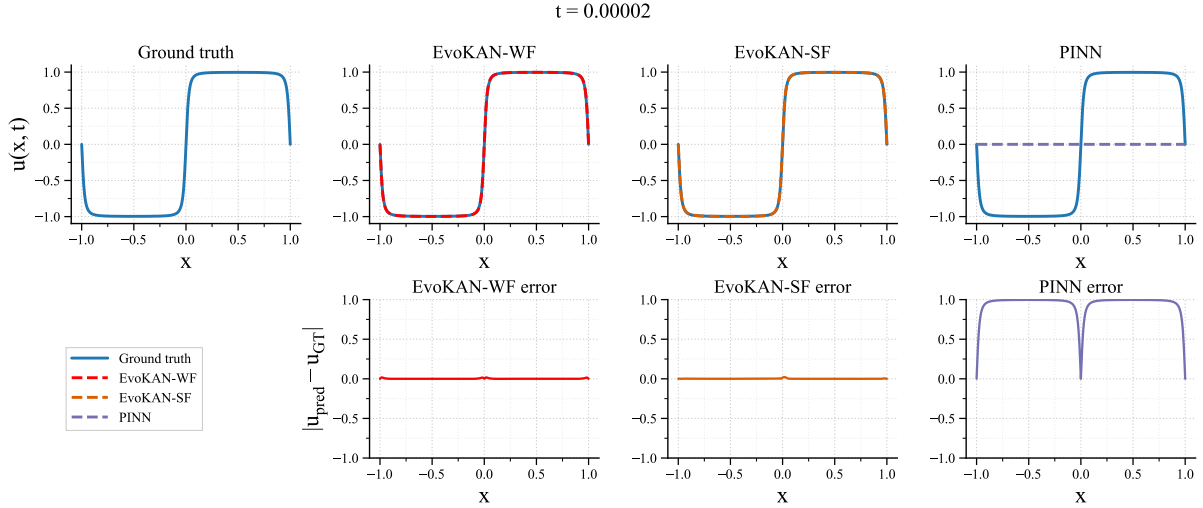


Figure 4: Comparison of predicted solutions for the one-dimensional Allen–Cahn equation (Eq. (41)) at $t = 2 \times 10^{-5}$, trained with 100 data points. Both EvoKAN–WF and EvoKAN–SF closely match the ground-truth solution at this time, whereas the vanilla PINN does not reproduce the correct profile.

To compare the predictive behavior of the different solvers, Figs. 4 and 5 present the numerical solutions of the one-dimensional Allen–Cahn equation at two representative time instances. At the earlier time ($t = 2 \times 10^{-5}$, Fig. 4), both EvoKAN–WF and EvoKAN–SF closely match the ground-truth solution, while the vanilla PINN does not accurately reproduce the profile. At the later time ($t = 5 \times 10^{-5}$, Fig. 5), as the solution becomes steeper, EvoKAN–WF maintains good agreement with the reference solution, whereas EvoKAN–SF exhibits localized deviations near the center and boundaries. The vanilla PINN again fails to capture the correct solution behavior. Overall, these results show that the weak-form evolutionary formulation provides stable and accurate predictions across the tested time instances, while the strong-form variant is slightly more sensitive to evolving solution gradients.

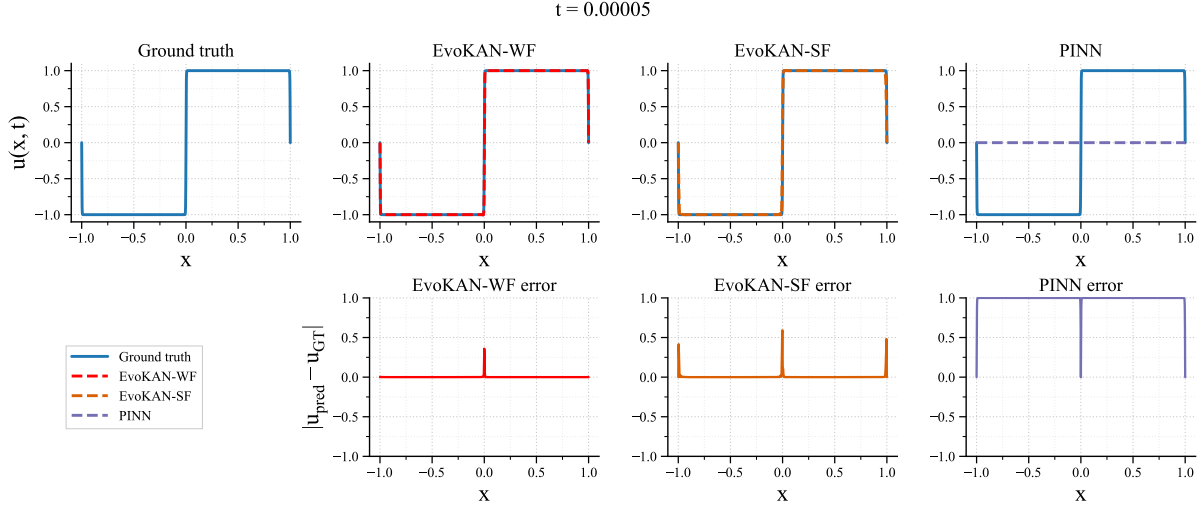


Figure 5: Comparison of predicted solutions for the one-dimensional Allen–Cahn equation (Eq. (41)) at $t = 5 \times 10^{-5}$, trained with 100 data points. As the solution profile becomes steeper, EvoKAN–WF maintains good accuracy, whereas EvoKAN–SF shows small deviations near the center and boundaries, and the vanilla PINN fails to recover the correct solution.

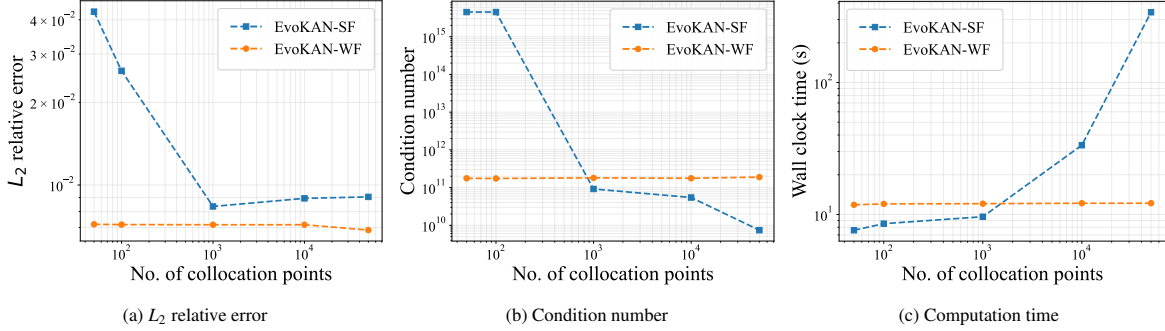


Figure 6: Strong-form (EvoKAN-SF) versus weak-form (EvoKAN-WF) evolutionary KAN solvers for the 1D Allen–Cahn equation (Eq. (41)) with respect to the number of collocation points: (a) L_2 relative error, (b) condition number, and (c) wall-clock time. The weak-form approach achieves lower errors and substantially better conditioning, while avoiding the rapid growth in computational cost observed in the strong-form solver.

To examine the effect of the number of collocation points on accuracy, conditioning, and computational cost, Figure 6 together with Table 3 summarizes the L_2 relative error, condition number, and wall clock time for EvoKAN SF and EvoKAN WF applied to the one dimensional Allen–Cahn equation. As the number of collocation points increases, EvoKAN SF shows a non monotonic error trend together with a growth of the condition number, which indicates ill conditioning of the parameter update system. In contrast, EvoKAN WF maintains low errors and a condition number that remains bounded across all tested resolutions, reflecting the decoupling between the update system size and the number of collocation points in the weak formulation. The computational cost of EvoKAN SF increases with the number of collocation points, whereas EvoKAN WF shows limited variation across all tested resolutions.

3.2. Dirichlet Boundary Condition: 2D Burgers' Equation

The two-dimensional vector Burgers' equation on a square domain is written in strong form as

$$\begin{cases} \frac{\partial u}{\partial t} = v \left(\frac{\partial^2 u}{\partial x^2} + \frac{\partial^2 u}{\partial y^2} \right) - \left(u \frac{\partial u}{\partial x} + v \frac{\partial u}{\partial y} \right), \\ \frac{\partial v}{\partial t} = v \left(\frac{\partial^2 v}{\partial x^2} + \frac{\partial^2 v}{\partial y^2} \right) - \left(u \frac{\partial v}{\partial x} + v \frac{\partial v}{\partial y} \right), \end{cases} \quad (x, y) \in \Omega, \quad t > 0, \quad (47)$$

where $u(x, y, t)$ and $v(x, y, t)$ denote the two velocity components and $\nu > 0$ is a constant viscosity. The computational domain is defined as

$$\Omega = (-1, 1) \times (-1, 1).$$

Table 3: L_2 relative error and wall clock time for the one-dimensional Allen–Cahn equation (Eq. (41)) with varying the number of collocation points. Speedup is defined as T_{SF}/T_{WF} . Entries marked with † correspond to EvoKAN-SF solutions whose L_2 relative error remains above $O(10^{-2})$, indicating insufficient accuracy.

Number of collocation points	L_2 relative error		Wall clock time		
	EvoKAN-SF	EvoKAN-WF	EvoKAN-SF [s]	EvoKAN-WF [s]	Speedup
64	4.2814e-02	7.1881e-03	7.4396 †	11.8412	0.63
100	2.6065e-02	7.1722e-03	8.5188 †	12.0379	0.71
1,000	8.3525e-03	7.1633e-03	16.1555	12.0761	1.34
10,000	8.9389e-03	7.1644e-03	33.5028	12.1654	2.76
50,000	9.0494e-03	6.8493e-03	340.6359	12.1727	27.99

The domain is equipped with homogeneous Dirichlet boundary conditions for both components,

$$u(x, y, t) = 0, \quad v(x, y, t) = 0, \quad (x, y) \in \partial\Omega, \quad t > 0. \quad (48)$$

To derive the weak formulation, a family of test functions $\{v_k\}_{k=1}^K$ is introduced. Each v_k is constructed from a Fourier sine basis with periods chosen so that $v_k = 0$ on $\partial\Omega$, thereby satisfying the homogeneous Dirichlet boundary condition by construction. Multiplying the first equation in (47) by v_k and integrating over Ω yields

$$\int_{\Omega} \frac{\partial u}{\partial t} v_k dx dy = \int_{\Omega} v \left(\frac{\partial^2 u}{\partial x^2} + \frac{\partial^2 u}{\partial y^2} \right) v_k dx dy - \int_{\Omega} \left(u \frac{\partial u}{\partial x} + v \frac{\partial u}{\partial y} \right) v_k dx dy.$$

The diffusion term is integrated by parts once, while the nonlinear advection term is left in advective form. Writing the Laplacian as $\Delta u = \nabla \cdot (\nabla u)$ and applying integration by parts gives

$$\int_{\Omega} v \Delta u v_k dx dy = - \int_{\Omega} v \nabla u \cdot \nabla v_k dx dy + \int_{\partial\Omega} v \frac{\partial u}{\partial n} v_k ds.$$

The boundary integral vanishes because the test functions are constructed from a Fourier sine basis whose period is chosen so that $v_k = 0$ on $\partial\Omega$. As a result, the trace of each test function is zero on the boundary, and the boundary contribution arising from integration by parts is eliminated. Substituting this expression back into the balance yields the weak form for the u -component,

$$\int_{\Omega} \frac{\partial u}{\partial t} v_k dx dy + \int_{\Omega} v \nabla u \cdot \nabla v_k dx dy + \int_{\Omega} \left(u \frac{\partial u}{\partial x} + v \frac{\partial u}{\partial y} \right) v_k dx dy = 0, \quad k = 1, \dots, K. \quad (49)$$

Applying the same procedure to the second equation in (47) gives

$$\int_{\Omega} \frac{\partial v}{\partial t} v_k dx dy = \int_{\Omega} v \left(\frac{\partial^2 v}{\partial x^2} + \frac{\partial^2 v}{\partial y^2} \right) v_k dx dy - \int_{\Omega} \left(u \frac{\partial v}{\partial x} + v \frac{\partial v}{\partial y} \right) v_k dx dy.$$

Integrating the diffusion term by parts yields

$$\int_{\Omega} v \Delta v v_k dx dy = - \int_{\Omega} v \nabla v \cdot \nabla v_k dx dy + \int_{\partial\Omega} v \frac{\partial v}{\partial n} v_k ds,$$

and the boundary contribution vanishes due to $v_k = 0$ on $\partial\Omega$. The resulting weak form for the v -component is

$$\int_{\Omega} \frac{\partial v}{\partial t} v_k dx dy + \int_{\Omega} v \nabla v \cdot \nabla v_k dx dy + \int_{\Omega} \left(u \frac{\partial v}{\partial x} + v \frac{\partial v}{\partial y} \right) v_k dx dy = 0, \quad k = 1, \dots, K. \quad (50)$$

Equations (49) and (50) together define the weak formulation of the two-dimensional Burgers' equation under homogeneous Dirichlet boundary conditions and form the basis for the numerical experiments.

The training settings for the two dimensional Burgers equation are summarized in Table 4. EvoKAN-WF and EvoKAN-SF use the same network architecture and are advanced in time using Adam with a fixed time step. PINN-SF employs a wider MLP with tanh activations and is trained using Adam and L-BFGS-B without time evolution.

To illustrate the effect of the weak formulation, Fig. 7 and Fig. 8 compare the predicted velocity magnitude fields for the two dimensional Burgers equation at $t = 0.1$ and $t = 0.4$, respectively. All models are trained using 900 collocation points. At both time instances, EvoKAN-WF reproduces the main flow structures observed

Table 4: Training configuration for the 2D Burgers equation (Eq. (47)).

	EvoKAN-WF	EvoKAN-SF	PINN-SF
Hidden layers	[16, 16, 16]	[16, 16, 16]	[25, 25, 25]
Activation functions	Gaussian RBFs/SiLU	Gaussian RBFs/SiLU	Tanh
Grid points number of activation functions	5	5	-
Number of trainable parameters	3392	3472	3670
Optimizer	Adam	Adam	Adam/L-BFGS-B
Timestep	1e-03	1e-03	-

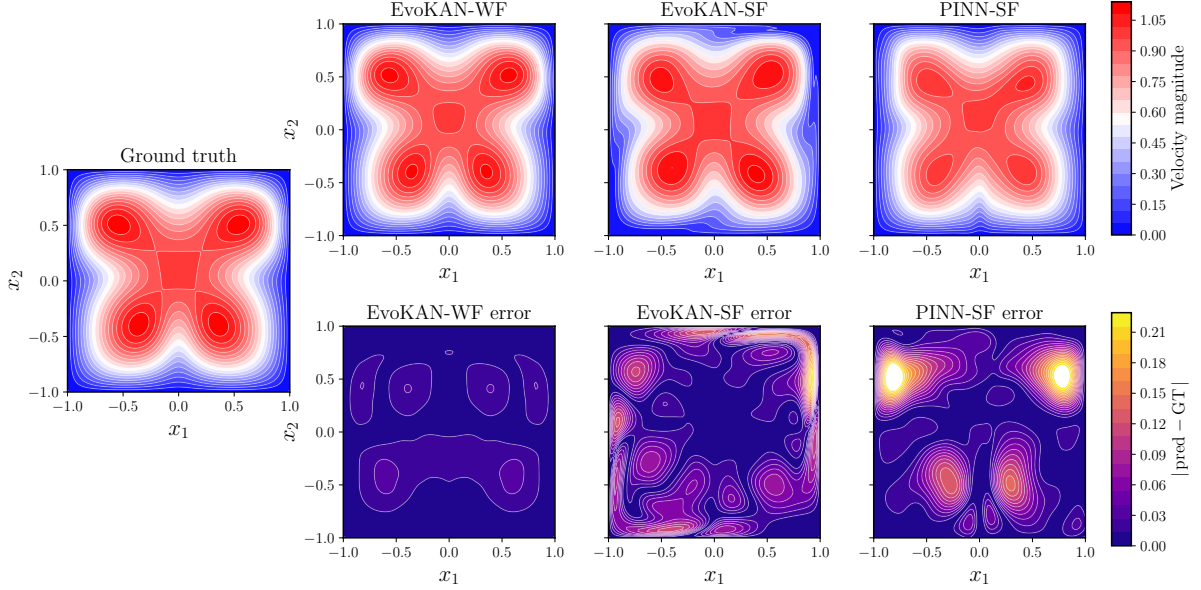


Figure 7: **Comparison of two-dimensional Burgers' equation (Eq. (47)) solutions at $t = 0.1$.** All models are trained using 900 collocation points. The top row shows the ground-truth FDM solution together with predictions from EvoKAN-WF, EvoKAN-SF, and PINN-SF. The bottom row presents the corresponding absolute error fields with respect to the ground truth. At this early time, EvoKAN-WF yields smaller errors than the other models while providing comparable representations of the overall flow structure.

in the reference FDM solution. The corresponding error fields remain spatially distributed without pronounced localization. EvoKAN-SF and PINN-SF predict the overall flow pattern, while exhibiting larger error amplitudes in regions associated with stronger velocity gradients. At the later time $t = 0.4$, differences between the methods become more apparent. EvoKAN-WF continues to represent the dominant flow features across the domain, whereas EvoKAN-SF and PINN-SF show increased discrepancies in localized regions. These results indicate that the weak-form formulation remains computationally efficient by maintaining predictive accuracy even with a relatively small number of collocation points, while preserving the global structure of the solution.

The quantitative trends observed in Fig. 9 are further supported by the numerical results reported in Table 5. For small sample sizes, EvoKAN-SF attains lower wall clock time but fails to achieve sufficient accuracy, as indicated by the large L_2 errors. As the number of collocation points increases, EvoKAN-WF consistently maintains lower errors while the computational cost remains nearly unchanged. In contrast, the wall clock time of EvoKAN-SF grows rapidly, leading to a substantial speedup in favor of EvoKAN-WF for moderate to large sample sizes. These results confirm the stable accuracy and favorable scaling behavior of the weak form approach for the two dimensional Burgers' equation.

3.3. 2D Heat Equation with Nonlinear Forcing Term

The two-dimensional heat equation with a nonlinear reaction term is written in strong form as

$$\frac{\partial u}{\partial t}(x, y, t) = \alpha \left(\frac{\partial^2 u}{\partial x^2}(x, y, t) + \frac{\partial^2 u}{\partial y^2}(x, y, t) \right) + u(t, x, y)(1 - u(x, y, t)), \quad (x, y) \in \Omega, \quad (51)$$

where the spatial domain is defined as $\Omega = (-1, 1)^2$ and $\alpha > 0$ denotes the diffusion coefficient. In the present numerical experiment, the diffusion coefficient is fixed to $\alpha = 0.1$ so that diffusion and nonlinear reaction act on comparable spatial and temporal scales.

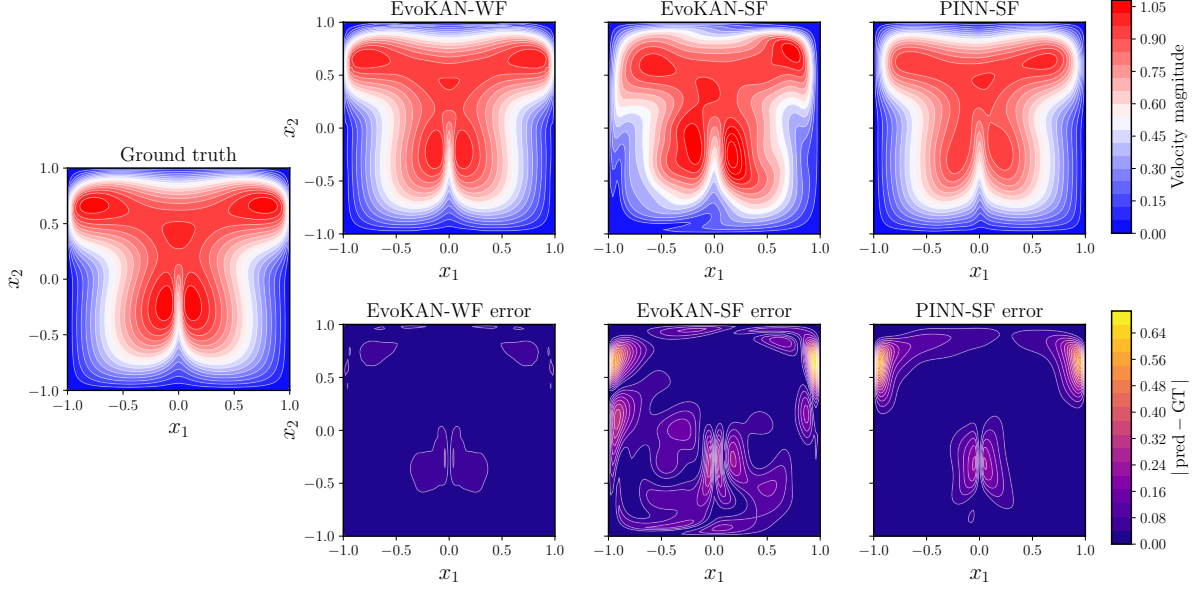


Figure 8: **Comparison of two-dimensional Burgers' equation (Eq. (47)) solutions at $t = 0.4$.** All models are trained using 900 collocation points. The top row shows the ground-truth FDM solution together with predictions from EvoKAN-WF, EvoKAN-SF, and PINN-SF. The bottom row presents the corresponding absolute error fields with respect to the ground truth. Despite the limited number of collocation samples, EvoKAN-WF provides more accurate predictions than the other models and better captures the flow structure across the domain.

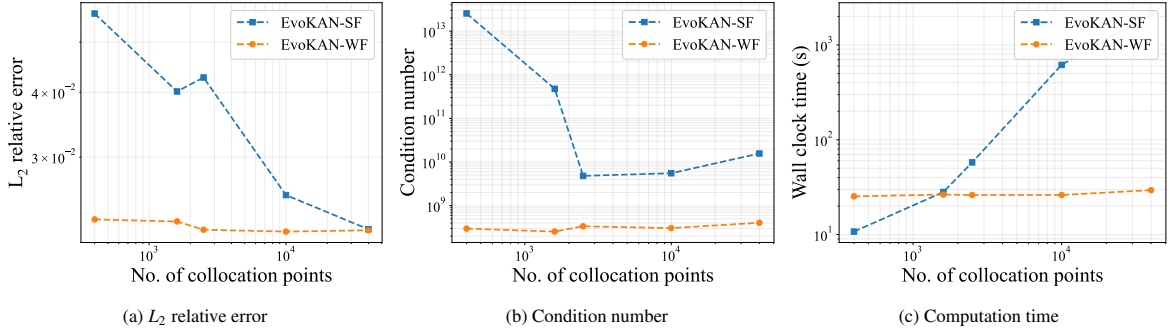


Figure 9: Strong-form (EvoKAN-SF) versus weak-form (EvoKAN-WF) evolutionary KAN solvers for the two-dimensional Burgers' equation (Eq. (47)) with respect to the number of collocation points: (a) L_2 relative error, (b) condition number, and (c) wall-clock time. The weak-form approach achieves lower errors and improved numerical conditioning, while avoiding the rapid growth in computational cost observed in the strong-form solver.

The initial condition prescribes the state at $t = 0$ as

$$u(x, y, 0) = \cos(\pi x) \cos(\pi y), \quad (x, y) \in \Omega, \quad (52)$$

and homogeneous Neumann boundary conditions enforce zero normal flux on the boundary $\partial\Omega$,

$$\frac{\partial u}{\partial n}(x, y, t) = 0, \quad (x, y) \in \partial\Omega, \quad t > 0, \quad (53)$$

where $\partial u/\partial n$ denotes the outward normal derivative.

To derive the weak formulation on Ω , a finite set of test functions $\{v_k(x, y)\}_{k=1}^K$ is introduced. Multiplying the strong form (51) by v_k and integrating over Ω yields

$$\int_{\Omega} u_t v_k d\Omega = \alpha \int_{\Omega} \Delta u v_k d\Omega + \int_{\Omega} u(1-u) v_k d\Omega. \quad (54)$$

Using integration by parts for the diffusion term gives

$$\int_{\Omega} \Delta u v_k d\Omega = \int_{\partial\Omega} \frac{\partial u}{\partial n} v_k d\Gamma - \int_{\Omega} \nabla u \cdot \nabla v_k d\Omega. \quad (55)$$

Table 5: L_2 relative error and wall clock time for the two-dimensional Burgers’ equation (Eq. (47)) with varying the number of collocation points. Speedup is defined as T_{SF}/T_{WF} . Entries marked with † correspond to EvoKAN-SF solutions whose L_2 relative error exceeds 5%, indicating insufficient accuracy.

Number of collocation points	L_2 relative error		Wall clock time		Speedup
	EvoKAN-SF	EvoKAN-WF	EvoKAN-SF [s]	EvoKAN-WF [s]	
900	5.67383e-02	2.27452e-02	10.7565 †	25.3241	0.42
1,600	4.01466e-02	2.25431e-02	28.1469	26.4252	1.07
2,500	4.27184e-02	2.17294e-02	57.7473	26.1492	2.21
10,000	2.53424e-02	2.15498e-02	617.0453	26.1723	23.58
40,000	2.17728e-02	2.16729e-02	2139.5068	29.4292	72.69

The boundary integral vanishes due to the homogeneous Neumann condition, and the weak form becomes

$$\int_{\Omega} u_t v_k d\Omega + \alpha \int_{\Omega} \nabla u \cdot \nabla v_k d\Omega - \int_{\Omega} u(1-u) v_k d\Omega = 0, \quad k = 1, \dots, K. \quad (56)$$

Table 6: Training configuration for the 2D Heat equation with nonlinear forcing term (Eq. (51)).

	EvoKAN-WF	EvoKAN-SF	PINN-SF
Hidden layers	[4, 4, 4]	[4, 4, 4]	[15, 15, 15]
Activation functions	Gaussian RBFs/SiLU	Gaussian RBFs/SiLU	Tanh
Grid points number of activation functions	8	5	-
Number of trainable parameters	388	388	526
Optimizer	Adam	Adam	Adam/L-BFGS-B
Timestep	1e-03	1e-03	-

Table 2 lists the training configurations used for EvoKAN-WF, EvoKAN-SF, and PINN-SF. The two evolutionary KAN models adopt an identical network design and undergo an initial optimization stage to fit the initial condition using the Adam optimizer. After this stage, the solution is advanced in time through parameter updates with a prescribed fixed time step. By contrast, PINN-SF relies on a deeper multilayer perceptron with tanh activations and is trained through standard optimization using Adam followed by L-BFGS-B, without a time marching mechanism.

To examine the solution behavior of different solvers for the two dimensional heat equation, Figs. 10 and 11 compare the predicted solutions and corresponding absolute error fields at $t = 0.20$ and $t = 0.50$ using the same number of collocation points. At both time instances, EvoKAN WF reproduces the main spatial features of the ground truth and yields error fields that remain smooth across the domain. EvoKAN SF shows localized error concentrations near regions with stronger spatial variation, while PINN SF also captures the overall solution structure and produces error fields that remain bounded under the same training setting. As time progresses from $t = 0.20$ to $t = 0.50$, the differences in error magnitude and spatial structure remain consistent across the two figures.

The dependence of solution accuracy, conditioning, and computational cost on the number of collocation points is summarized in Fig. 12 for EvoKAN SF and EvoKAN WF applied to the two dimensional heat equation. As the number of collocation points increases, EvoKAN SF exhibits variations in the L2 relative error together with an increase in the condition number. EvoKAN WF maintains lower error levels and a condition number that remains bounded across the tested resolutions. The wall clock time increases with the number of collocation points for EvoKAN SF, whereas EvoKAN WF shows a weaker dependence on the collocation count.

The evolution of boundary gradient errors over time for the two dimensional heat equation is reported in Fig. 13 for EvoKAN WF, EvoKAN SF, and PINN SF. Across all four boundaries, EvoKAN WF shows a consistent decrease in the average gradient error as time progresses. The error curves remain smooth and follow a monotonic decay pattern during the time evolution. EvoKAN SF exhibits slower error reduction and maintains higher boundary errors over the same time interval. PINN SF captures the general trend of error decay but shows larger temporal variations and higher error levels on all boundaries. These results indicate that the weak formulation provides a stable treatment of Neumann boundary conditions and leads to more controlled boundary error evolution under the same training setting.

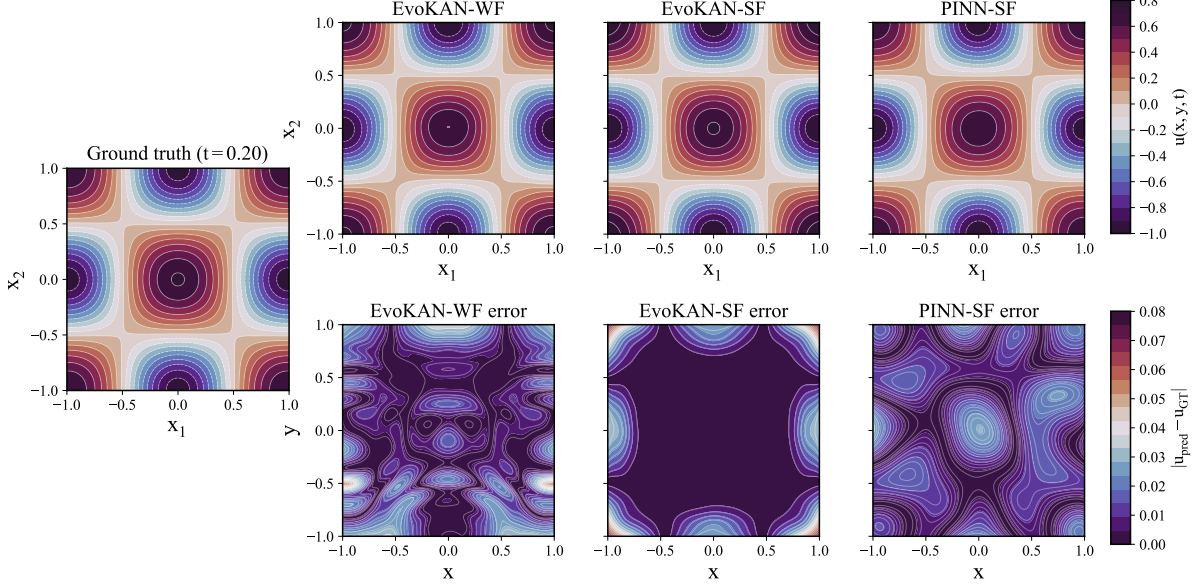


Figure 10: **Comparison of two-dimensional heat equation (Eq. (51)) solutions at $t = 0.20$.** All models are trained using 400 collocation points. The top row shows the ground-truth solution together with predictions from EvoKAN-WF, EvoKAN-SF, and PINN-SF. The bottom row presents the corresponding absolute error fields with respect to the ground truth. The weak-form solver (EvoKAN-WF) exhibits smoother error distributions and reduced boundary artifacts compared to the strong-form approaches under the same training budget.

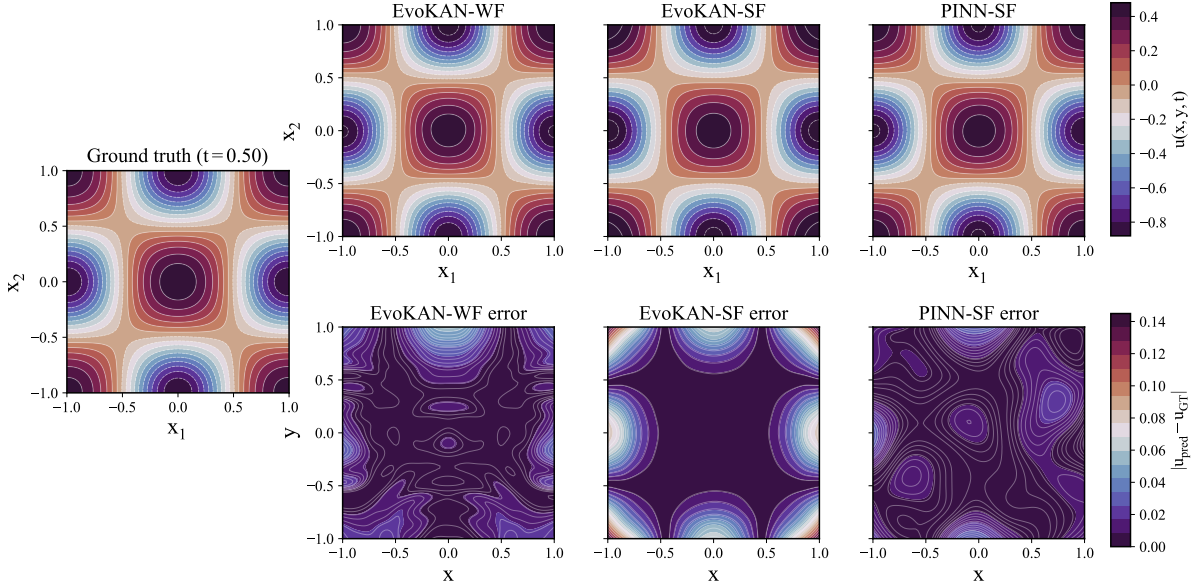


Figure 11: **Comparison of two-dimensional heat equation solutions at $t = 0.50$.** All models are trained using 400 collocation points. The top row presents the ground-truth solution along with predictions obtained by EvoKAN-WF, EvoKAN-SF, and PINN-SF. The bottom row displays the corresponding absolute error fields relative to the ground truth. Even at this later time, the weak-form solver (EvoKAN-WF) maintains higher accuracy, exhibiting consistently lower errors and smoother spatial error patterns than the strong-form approaches under the same training budget.

3.4. Periodic Boundary Condition: 2D Porous Medium Equation with Drift

The two-dimensional porous medium equation with drift is written in strong form as

$$\frac{\partial u}{\partial t} = \nabla \cdot (\nabla(u^2)) - \nabla \cdot (\mathbf{V}(x, y) u), \quad (x, y) \in \Omega, \quad t > 0, \quad (57)$$

with nonlinear diffusion exponent fixed at $m = 2$. The drift velocity field is prescribed by

$$\mathbf{V}(x, y) = \begin{pmatrix} \pi \cos(\pi x) \sin(\pi y) \\ \pi \sin(\pi x) \cos(\pi y) \end{pmatrix} = \nabla(\sin(\pi x) \sin(\pi y)), \quad (58)$$

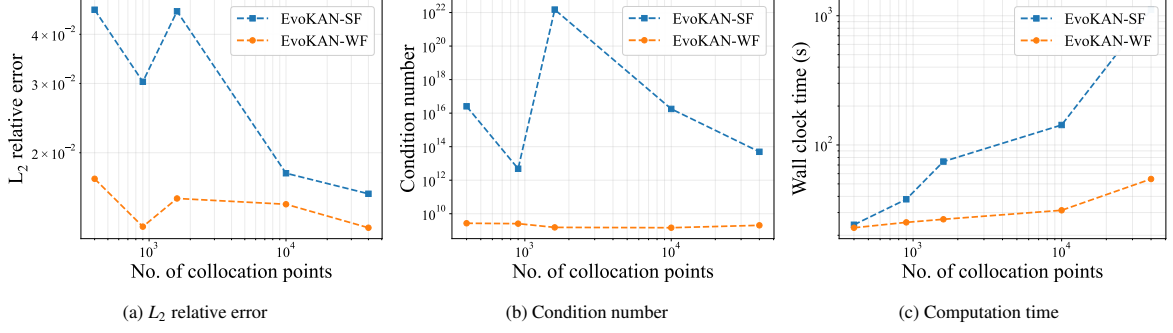


Figure 12: Strong-form (EvoKAN-SF) versus weak-form (EvoKAN-WF) evolutionary KAN solvers for the two-dimensional heat equation with respect to the number of collocation points: (a) L_2 relative error, (b) condition number, and (c) wall-clock time. The weak-form approach achieves lower errors and substantially better conditioning, while avoiding the rapid growth in computational cost observed in the strong-form solver.

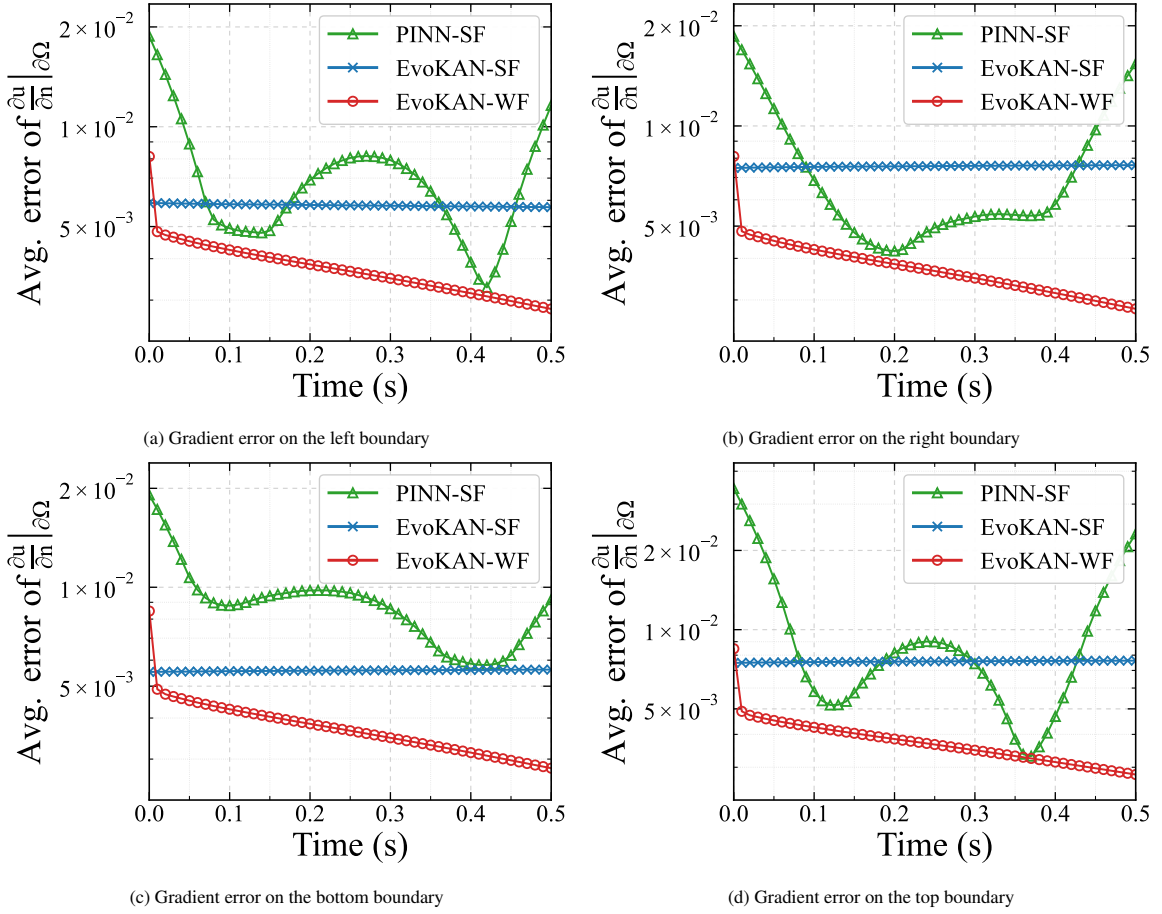


Figure 13: Gradient error on each boundary for the 2D heat equation (Eq. (51)). The weak form evolutionary KAN progressively reduces the gradient error as the time evolution proceeds and the error approaches zero along all boundaries. The weak formulation provides stable treatment of the Neumann boundary condition and enables monotonic error reduction during network updates. The strong-form evolutionary network enforces a constant-derivative boundary condition, making convergence of the boundary error to zero difficult, while the strong-form PINN exhibits oscillatory boundary errors during the time evolution.

so that the transport term follows a potential flow. The computational domain is defined as

$$\Omega = (-1, 1) \times (-1, 1).$$

The problem is equipped with periodic boundary conditions in both spatial directions,

$$u(-1, y, t) = u(1, y, t), \quad u(x, -1, t) = u(x, 1, t),$$

together with periodicity of the associated fluxes.

Table 7: L_2 relative error and wall-clock time for the two-dimensional heat equation (Eq. (51)) with varying numbers of collocation points. Speedup is defined as T_{SF}/T_{WF} .

Number of collocation points	L_2 relative error		Wall-clock time		
	EvoKAN-SF	EvoKAN-WF	EvoKAN-SF [s]	EvoKAN-WF [s]	Speedup
400	4.6195e-02	1.7171e-02	24.1326	22.8757	1.06
900	3.0303e-02	1.2976e-02	37.9921	25.1838	1.51
1,600	4.5767e-02	1.5302e-02	74.4028	26.6005	2.80
10,000	1.7737e-02	1.4792e-02	142.7417	31.2263	4.57
40,000	1.5728e-02	1.2892e-02	1111.4212	54.5341	20.39

To derive the weak formulation, a family of test functions $\{v_k\}_{k=1}^K$ is introduced. Each test function is defined using trigonometric Fourier modes of the form $\cos(m\pi x)$ or $\sin(m\pi x)$ with mode index $m = 1, 2, \dots$ in each spatial direction. The mode indices are chosen to satisfy periodicity on $\partial\Omega$, and the constant mode is excluded to avoid redundancy in the test space. Multiplying (57) by v_k and integrating over Ω yields

$$\int_{\Omega} \left(\frac{\partial u}{\partial t} - \nabla \cdot (\nabla(u^2)) + \nabla \cdot (\mathbf{V}u) \right) v_k dx dy = 0, \quad k = 1, \dots, K. \quad (59)$$

The divergence terms are treated by integration by parts. For the nonlinear diffusion term,

$$- \int_{\Omega} \nabla \cdot (\nabla(u^2)) v_k dx dy = \int_{\Omega} \nabla(u^2) \cdot \nabla v_k dx dy - \int_{\partial\Omega} \nabla(u^2) \cdot \mathbf{n} v_k ds,$$

and for the drift term,

$$\int_{\Omega} \nabla \cdot (\mathbf{V}u) v_k dx dy = - \int_{\Omega} (\mathbf{V}u) \cdot \nabla v_k dx dy + \int_{\partial\Omega} (\mathbf{V}u) \cdot \mathbf{n} v_k ds,$$

where \mathbf{n} denotes the outward unit normal on $\partial\Omega$. The boundary integrals cancel under periodic boundary conditions because opposite sides of the domain contribute equal and opposite flux terms. Substituting these relations into the integral balance yields the weak form

$$\int_{\Omega} \frac{\partial u}{\partial t} v_k dx dy = - \int_{\Omega} \nabla(u^2) \cdot \nabla v_k dx dy + \int_{\Omega} (\mathbf{V}u) \cdot \nabla v_k dx dy, \quad k = 1, \dots, K. \quad (60)$$

Equation (60) defines the weak formulation of the porous medium equation with drift under periodic boundary conditions and serves as the spatial weak form for the numerical experiments.

Table 8: Training configuration for the 2D porous medium equation with drift (Eq. (57)).

	EvoKAN-WF	EvoKAN-SF	PINN-SF
Hidden layers	[7, 7, 7]	[7, 7, 7]	[15, 15, 15]
Activation functions	Gaussian RBFs/SiLU	Gaussian RBFs/SiLU	Tanh
Grid points number of activation functions	5	5	-
Number of trainable parameters	770	770	526
Optimizer	Adam	Adam	Adam/L-BFGS-B
Timestep	1e-03	1e-03	-

The solution fields for the two dimensional porous medium equation with drift under periodic boundary conditions are shown in Fig. 14. At the initial time $t = 0$, all methods reproduce the prescribed initial distribution. At the final time $t = 0.4$, EvoKAN-WF, EvoKAN-SF, and PINN capture the large scale transport patterns induced by the combined nonlinear diffusion and drift. The spatial structures remain periodic across the domain, reflecting consistent enforcement of the periodic boundary conditions. Under the same number of collocation points and time step, the predicted solution fields exhibit comparable global behavior while differing in the smoothness of local variations.

The dependence of conditioning and computational cost on the number of collocation points for the two dimensional porous medium equation is shown in Fig. 15. As the sample size increases, EvoKAN-SF exhibits a pronounced increase in the condition number together with a rapid growth in wall clock time. In contrast, EvoKAN-WF maintains controlled conditioning and a gradual increase in computational cost. These results indicate that the

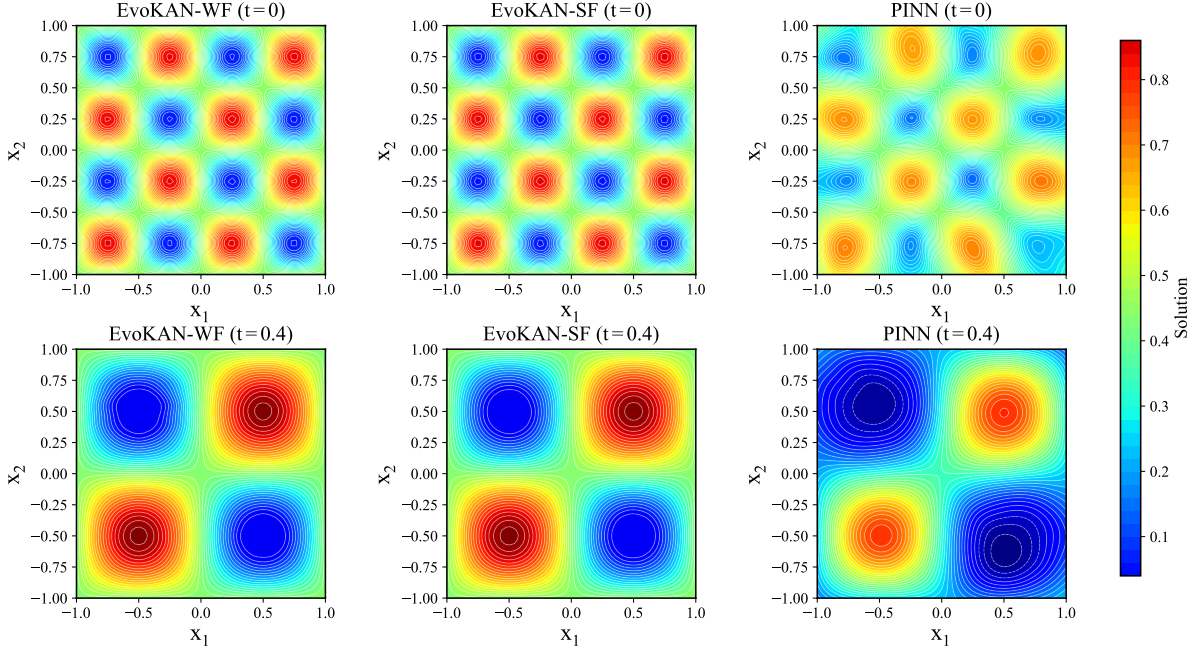


Figure 14: **Solution field comparison for the two-dimensional PME with drift under periodic boundary conditions (Eq. (57))**. The solution fields at $t = 0$ (top row) and $t = 0.4$ (bottom row) are shown for EvoKAN-WF, EvoKAN-SF, and PINN, respectively. All models are trained using $N_c = 3600$ collocation points, with a uniform time step $\Delta t = 10^{-2}$ up to the final time $T = 0.4$. The color map represents the spatial distribution of the solution $u(x_1, x_2, t)$, illustrating the nonlinear diffusion and drift-induced transport dynamics.

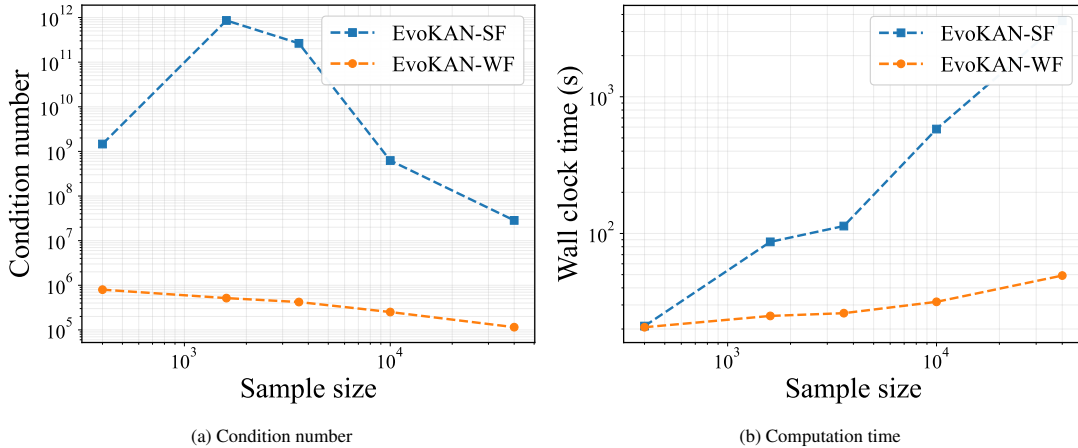


Figure 15: Strong-form (EvoKAN-SF) versus weak-form (EvoKAN-WF) evolutionary KAN solvers for the two-dimensional porous medium equation (Eq. (57)) with respect to the number of collocation points: (a) condition number and (b) wall-clock time. The weak-form approach achieves substantially better conditioning while avoiding the rapid growth in computational cost observed in the strong-form solver.

weak form formulation leads to more stable parameter update systems and more favorable computational scaling than the strong form approach for this problem.

The energy evolution for the two dimensional porous medium equation is shown in Fig. 16 for different numbers of collocation points. In the case of 400 collocation points, EvoKAN-SF exhibits a temporary increase in energy, indicating that the solution does not follow the expected dissipative behavior. For 1600 collocation points, the energy decay of EvoKAN-SF remains incomplete over the simulated time interval. Only when 3600 collocation points are employed does EvoKAN-SF exhibit monotone energy decay. In contrast, EvoKAN-WF shows consistent energy decay for all tested resolutions. This behavior indicates that the weak form formulation preserves the dissipative structure of the porous medium equation with reduced sensitivity to the number of collocation points.

The solution validity and computational cost are summarized in Table 9. For smaller numbers of collocation points, EvoKAN-SF fails to produce a valid solution, as indicated by non-decreasing or incomplete energy decay, whereas EvoKAN-WF yields admissible solutions in all tested cases. As the number of collocation points

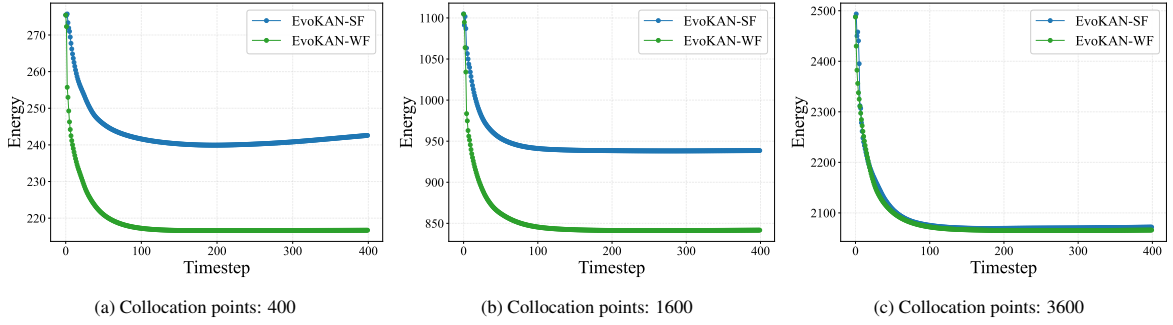


Figure 16: Energy evolution of strong-form (EvoKAN-SF) and weak-form (EvoKAN-WF) evolutionary KAN solvers for the two-dimensional porous medium equation under different numbers of collocation points. For EvoKAN-SF, monotone energy decay is observed only when a sufficiently large number of collocation points is used. At lower resolutions, EvoKAN-SF exhibits energy increase or incomplete decay over time. In contrast, EvoKAN-WF shows consistent energy decay across all tested resolutions.

Table 9: Solution validity and wall clock time for the 2D PME (Eq. (57)) with varying the number of collocation points. The solution validity indicator reports whether the numerical solution exhibits a dissipative energy evolution consistent with the governing equation. Entries marked with \times correspond to cases where the computed energy shows non-decreasing behavior or incomplete decay over the simulated time interval, indicating that the solution does not provide an admissible approximation under the given discretization. Speedup is defined as T_{SF}/T_{WF} .

Number of collocation points	Approximation validity		Wall clock time		
	EvoKAN-SF	EvoKAN-WF	EvoKAN-SF [s]	EvoKAN-WF [s]	Speedup
400	\times	\circ	21.0145	20.6104	1.02
1,600	\times	\circ	86.8148	24.9313	3.48
3,600	\circ	\circ	113.3219	26.1163	4.34
10,000	\circ	\circ	580.5136	31.6187	18.37
40,000	\circ	\circ	3599.2407	49.2156	73.12

increases, both methods produce valid solutions, but the wall clock time of EvoKAN-SF increases rapidly. In contrast, EvoKAN-WF maintains a lower computational cost, leading to increasing speedup as the sample size grows.

4. Conclusion

This work presents a weak-form evolutionary Kolmogorov–Arnold network framework for solving PDEs. The main contributions of this work are threefold: (i) the proposed formulation constructs parameter update systems whose size is fixed by the number of test functions and remains independent of the number of training samples, enabling scalable computational efficiency; (ii) by replacing pointwise residual evaluation with weak residual projections and reducing the order of differentiation, the method produces well-conditioned linear systems and maintains accuracy for solutions approaching discontinuities; and (iii) Dirichlet and periodic boundary conditions are enforced through boundary-constrained trial spaces, while Neumann conditions are incorporated directly into the weak formulation via integration by parts.

The numerical results demonstrate consistent differences between weak-form and strong-form evolutionary solvers across multiple benchmark problems. For the one-dimensional Allen–Cahn equation (Figs. 4, 5 and Table 3), the weak-form solver maintained accurate interface evolution and bounded condition numbers even with very few collocation points, while the strong-form solver exhibited accuracy degradation and ill-conditioning at low resolutions. For the two-dimensional heat equation with Neumann boundary conditions (Figs. 10–12), the weak-form formulation produced lower L_2 errors and smoother error fields under the same training budget, and enabled stable reduction of boundary gradient errors during time evolution (Fig. 13).

In the two-dimensional Burgers’ equation (Figs. 7–9), the weak-form evolutionary solver preserved the global flow structure under limited collocation data and achieved lower errors than strong-form evolutionary solvers. As the number of collocation points increased, the computational cost of the strong-form solver grew rapidly, whereas the weak-form solver showed weak dependence on the sample size. For the two-dimensional porous medium equation with drift (Figs. 16 and Table 9), the weak-form solver consistently produced solutions with dissipative energy evolution across all tested resolutions, while the strong-form solver required sufficiently large collocation sets to recover admissible energy decay.

Overall, the weak-form evolutionary framework enables accurate resolution of complex physical phenomena with controlled conditioning and stable time evolution, even under limited computational resources. Future work will investigate uncertainty quantification and applications to practical engineering systems, extending the present framework toward realistic, data-constrained physical problems.

Acknowledgment

We would like to thank the support of National Science Foundation (DMS-2533878, DMS-2053746, DMS-2134209, ECCS-2328241, CBET-2347401 and OAC-2311848), and U.S. Department of Energy (DOE) Office of Science Advanced Scientific Computing Research program DE-SC0023161, the SciDAC LEADS Institute, and DOE–Fusion Energy Science, under grant number: DE-SC0024583.

References

- [1] Bing Yu et al. The deep ritz method: a deep learning-based numerical algorithm for solving variational problems. *Communications in Mathematics and Statistics*, 6(1):1–12, 2018.
- [2] E Weinan. Machine learning and computational mathematics. *arXiv preprint arXiv:2009.14596*, 2020.
- [3] Jiequn Han, Arnulf Jentzen, and Weinan E. Solving high-dimensional partial differential equations using deep learning. *Proceedings of the National Academy of Sciences*, 115(34):8505–8510, 2018.
- [4] Justin Sirignano and Konstantinos Spiliopoulos. Dgm: A deep learning algorithm for solving partial differential equations. *Journal of Computational Physics*, 375:1339–1364, 2018.
- [5] George Em Karniadakis, Ioannis G Kevrekidis, Lu Lu, Paris Perdikaris, Sifan Wang, and Liu Yang. Physics-informed machine learning. *Nature Reviews Physics*, 3(6):422–440, 2021.
- [6] Shengze Cai, Zhiping Mao, Zhicheng Wang, Minglang Yin, and George Em Karniadakis. Physics-informed neural networks (pinns) for fluid mechanics: A review. *Acta Mechanica Sinica*, 37(12):1727–1738, 2021.
- [7] Maziar Raissi, Paris Perdikaris, and George E Karniadakis. Physics-informed neural networks: A deep learning framework for solving forward and inverse problems involving nonlinear partial differential equations. *Journal of Computational physics*, 378:686–707, 2019.
- [8] Chenxi Wu, Min Zhu, Qinyang Tan, Yadhu Kartha, and Lu Lu. A comprehensive study of non-adaptive and residual-based adaptive sampling for physics-informed neural networks. *Computer Methods in Applied Mechanics and Engineering*, 403:115671, 2023.
- [9] Zhiping Mao and Xuhui Meng. Physics-informed neural networks with residual/gradient-based adaptive sampling methods for solving partial differential equations with sharp solutions. *Applied Mathematics and Mechanics*, 44(7):1069–1084, 2023.
- [10] Ameya D. Jagtap and George Em Karniadakis. Extended physics-informed neural networks (xpinns): A generalized space-time domain decomposition based deep learning framework for nonlinear partial differential equations. *Communications in Computational Physics*, 28(5):2002–2041, 2020.
- [11] Khemraj Shukla, Ameya D. Jagtap, and George Em Karniadakis. Parallel physics-informed neural networks via domain decomposition. *Journal of Computational Physics*, 447:110683, 2021.
- [12] Sifan Wang, Hanwen Wang, and Paris Perdikaris. On the eigenvector bias of fourier feature networks: From regression to solving multi-scale pdes with physics-informed neural networks. *Computer Methods in Applied Mechanics and Engineering*, 384:113938, 2021.
- [13] Wei Cai and Zhi-Qin John Xu. Multi-scale deep neural networks for solving high dimensional pdes. *arXiv preprint arXiv:1910.11710*, 2019.
- [14] Guofei Pang, Lu Lu, and George Em Karniadakis. fpinns: Fractional physics-informed neural networks. *SIAM Journal on Scientific Computing*, 41(4):A2603–A2626, 2019.
- [15] Lu Lu, Pengzhan Jin, and George Em Karniadakis. Learning nonlinear operators via deeponet based on the universal approximation theorem of operators. *Nature Machine Intelligence*, 3:218–229, 2021.

- [16] Zongyi Li, Nikola Kovachki, Kamyar Azizzadenesheli, and Anima Anandkumar. Fourier neural operator for parametric partial differential equations. In *ICLR*, 2021.
- [17] Nikola Kovachki et al. Neural operator: A learning framework for operators. *arXiv:2108.08481*, 2021.
- [18] Yunan Cao, Zongyi Li, Kamyar Azizzadenesheli, and Anima Anandkumar. Laplacian neural operator: Learning stable pde solvers with implicit layers. *NeurIPS*, 2023.
- [19] Atul Garg, Bobby Mallick, and George Em Karniadakis. Neuroscience-inspired neural operator for partial differential equations. *Journal of Computational Physics*, 500:112809, 2024.
- [20] Yiyuan Chen, Lu Lu, and George Em Karniadakis. Neural dynamical operator: Continuous spatial–temporal model with gradient-based and derivative-free optimization methods. *Journal of Computational Physics*, 514:113190, 2025.
- [21] Ziming Liu, Yixuan Wang, Sachin Vaidya, Fabian Ruehle, James Halverson, Marin Soljačić, Thomas Y Hou, and Max Tegmark. Kan: Kolmogorov-arnold networks. *arXiv preprint arXiv:2404.19756*, 2024.
- [22] Ziming Liu, Pingchuan Ma, Yixuan Wang, Wojciech Matusik, and Max Tegmark. Kan 2.0: Kolmogorov-arnold networks meet science. *arXiv preprint arXiv:2408.10205*, 2024.
- [23] Andrei Nikolaevich Kolmogorov. On the representation of continuous functions of many variables by superposition of continuous functions of one variable and addition. In *Doklady Akademii Nauk*, volume 114, pages 953–956. Russian Academy of Sciences, 1957.
- [24] Andrei Nikolaevich Kolmogorov. *On the representation of continuous functions of several variables by superpositions of continuous functions of a smaller number of variables*. American Mathematical Society, 1961.
- [25] Jürgen Braun and Michael Griebel. On a constructive proof of kolmogorov’s superposition theorem. *Constructive approximation*, 30:653–675, 2009.
- [26] Andrea Apicella, Francesco Donnarumma, Francesco Isgrò, and Roberto Prevete. A survey on modern trainable activation functions. *Neural Networks*, 138:14–32, 2021.
- [27] Edmondo Trentin. Networks with trainable amplitude of activation functions. *Neural Networks*, 14(4-5):471–493, 2001.
- [28] Diab W Abueidda, Panos Pantidis, and Mostafa E Mobasher. Deepokan: Deep operator network based on kolmogorov arnold networks for mechanics problems. *arXiv preprint arXiv:2405.19143*, 2024.
- [29] Yizheng Wang, Jia Sun, Jinshuai Bai, Cosmin Anitescu, Mohammad Sadegh Eshaghi, Xiaoying Zhuang, Timon Rabczuk, and Yinghua Liu. Kolmogorov–arnold-informed neural network: A physics-informed deep learning framework for solving forward and inverse problems based on kolmogorov–arnold networks. *Computer Methods in Applied Mechanics and Engineering*, 433:117518, 2025.
- [30] Prakash Thakolkaran, Yaqi Guo, Shivam Saini, Mathias Peirlinck, Benjamin Alheit, and Siddhant Kumar. Can kan cans? input-convex kolmogorov-arnold networks (kans) as hyperelastic constitutive artificial neural networks (cans). *Computer Methods in Applied Mechanics and Engineering*, 443:118089, 2025.
- [31] Yifan Du and Tamer A Zaki. Evolutional deep neural network. *Physical Review E*, 104(4):045303, 2021.
- [32] Jiahao Zhang, Shiheng Zhang, Jie Shen, and Guang Lin. Energy-dissipative evolutionary deep operator neural networks. *Journal of Computational Physics*, 498:112638, 2024.
- [33] Guang Lin, Changhong Mou, and Jiahao Zhang. Energy-dissipative evolutionary kolmogorov-arnold networks for complex pde systems. *arXiv preprint arXiv:2503.01618*, 2025.
- [34] Bongseok Kim, Jiahao Zhang, and Guang Lin. Bekan: Boundary condition-guaranteed evolutionary kolmogorov-arnold networks with radial basis functions for solving pde problems. *arXiv preprint arXiv:2510.03576*, 2025.
- [35] Tim De Ryck, Siddhartha Mishra, and Roberto Molinaro. wpinns: Weak physics informed neural networks for approximating entropy solutions of hyperbolic conservation laws. *SIAM Journal on Numerical Analysis*, 62(2):811–841, 2024.

- [36] Xianke Wang, Shichao Yi, Huangliang Gu, Jing Xu, and Wenjie Xu. Wf-pinns: solving forward and inverse problems of burgers equation with steep gradients using weak-form physics-informed neural networks. *Scientific Reports*, 15(1):40555, 2025.
- [37] Rui Xu, Dongxiao Zhang, Miao Rong, and Nanzhe Wang. Weak form theory-guided neural network (tgnn-wf) for deep learning of subsurface single-and two-phase flow. *Journal of Computational Physics*, 436:110318, 2021.
- [38] Ehsan Kharazmi, Zhongqiang Zhang, and George Em Karniadakis. Variational physics-informed neural networks for solving partial differential equations. *arXiv preprint arXiv:1912.00873*, 2019.
- [39] Somdatta Goswami, Minglang Yin, Yue Yu, and George Em Karniadakis. A physics-informed variational deeponet for predicting crack path in quasi-brittle materials. *Computer Methods in Applied Mechanics and Engineering*, 391:114587, 2022.
- [40] Stefano Berrone, Claudio Canuto, Moreno Pintore, and Natarajan Sukumar. Enforcing dirichlet boundary conditions in physics-informed neural networks and variational physics-informed neural networks. *Heliyon*, 9(8), 2023.
- [41] Vivienne Sze, Yu-Hsin Chen, Tien-Ju Yang, and Joel S Emer. Efficient processing of deep neural networks: A tutorial and survey. *Proceedings of the IEEE*, 105(12):2295–2329, 2017.
- [42] Daniele Fakhoury, Emanuele Fakhoury, and Hendrik Speleers. Exspline: An interpretable and expressive spline-based neural network. *Neural Networks*, 152:332–346, 2022.
- [43] Mario Köppen. On the training of a kolmogorov network. In *Artificial Neural Networks ICANN 2002: International Conference Madrid, Spain, August 28–30, 2002 Proceedings 12*, pages 474–479. Springer, 2002.
- [44] Ji-Nan Lin and Rolf Unbehauen. On the realization of a kolmogorov network. *Neural Computation*, 5(1):18–20, 1993.
- [45] Ming-Jun Lai and Zhaiming Shen. The kolmogorov superposition theorem can break the curse of dimensionality when approximating high dimensional functions. *arXiv preprint arXiv:2112.09963*, 2021.
- [46] Pierre-Emmanuel Leni, Yohan D Fougere, and Frédéric Truchetet. The kolmogorov spline network for image processing. In *Image Processing: Concepts, Methodologies, Tools, and Applications*, pages 54–78. IGI Global, 2013.
- [47] Juncai He. On the optimal expressive power of relu dnns and its application in approximation with kolmogorov superposition theorem. *arXiv preprint arXiv:2308.05509*, 2023.
- [48] Z Li. Kolmogorov-arnold networks are radial basis function networks. arxiv 2024. *arXiv preprint arXiv:2405.06721*, 2024.
- [49] Mark JL Orr et al. Introduction to radial basis function networks, 1996.
- [50] Martin Dietrich Buhmann. Radial basis functions. *Acta numerica*, 9:1–38, 2000.
- [51] Maziar Raissi, Paris Perdikaris, and George Karniadakis. Physics-informed neural networks: A deep learning framework for solving forward and inverse problems involving nonlinear partial differential equations. *Journal of Computational Physics*, 378:686–707, 2019.